

Partial Equilibration Scenario in 3D athermal martensites quenched below first-order transition temperatures

N. Shankaraiah¹, K.P.N. Murthy² and S.R. Shenoy¹

¹Tata Institute of Fundamental Research-Hyderabad, Hyderabad, Telangana 500046, India.

²Dept of Physics, Central University of Rajasthan, Bandar Sindri, Rajasthan 305817, India
(Dated: October 6, 2022)

To test a Partial Equilibration Scenario (PES) of Ritort and colleagues, we do Monte Carlo simulations of discretized-strain spin models, for four 3D martensitic structural transitions under quenches to a bath temperature $T < T_0$ below a first-order transition. The ageing system faces entropy barriers, in *searches* for energy-lowering passages between quasi-microcanonical energy shells. We confirm the PES signature of an exponential-tail distribution of intermittent heat releases to the bath, scaled in an effective temperature, that in our case, depends on the quench. When its inverse $\beta_{eff}(T) \equiv 1/T_{eff}(T)$ vanishes below a ‘martensite start’ temperature T_1 of avalanche conversions, then entropy barriers vanish. When this search temperature $T_{eff}(T)$ vanishes, PES cooling is arrested, as entropy barriers diverge. We find a *linear* vanishing of $T_{eff}(T) \sim T_d - T$, below a delay-divergence temperature T_d in between, $T_1 < T_d < T_0$. Martensitic conversion delays $e^{1/T_{eff}} \sim e^{1/(T_d - T)}$ thus have Vogel-Fulcher-Tammann like divergences. Post-quench delay data extracted from simulations and athermal martensitic alloys, are both consistent with predictions.

I. INTRODUCTION

The re-equilibration of a system after a quench is a long-standing problem in non-equilibrium statistical mechanics, and a generic Partial Equilibration Scenario (PES) has been proposed by Ritort and colleagues¹⁻⁴. After a quench, the system spreads rapidly over an energy shell E in configuration space. The system lowers its energy by intermittent energy releases $\delta E < 0$ to the heat bath at T , and then again spreads ergodically over the next energy shell $E' = E + \delta E < E$. The iteration of the fast/ slow steps ratchets the system down to a canonical equilibrium at T . The distribution of energy changes $\{\delta E\}$ has a signature exponential tail¹⁻⁴ in the heat release distribution $P_0(\delta E; t_w) \sim e^{\delta E/2T_{eff}(t_w)}$, whose slope at the origin defines the (inverse) effective temperature $\beta_{eff} \equiv 1/T_{eff}$, dependent on the post-quench waiting time t_w . The tail for negative energies is part of a shifted gaussian that peaks at positive energies. The PES has been confirmed through analytic Monte Carlo (MC) calculations of relaxing independent harmonic oscillators^{1,2}; by simulations of spin-glass models and Lennard-Jones binary mixtures^{3,4}, and through voltage noise intermittency³. The MC updates of ageing harmonic oscillators² have to hit the ever-shrinking target of as yet unrelaxed oscillators, and these rising entropy barriers induce slow decreases in energies $1/\ln t$ and acceptances $\sim 1/t \ln t$.

It is natural to test PES ideas in interacting systems with slow relaxations. The structural glass transition⁵ is an attempted equilibration that is arrested at a glassy freezing temperature T_G , pre-empting crystallization^{5,6}. The T -dependent effective viscosity increases above a Vogel-Fulcher-Tammann (VFT) singularity^{7,8} $e^{1/|T - T_G|}$, that has been studied for a century, but is not yet fully understood. Further, decays around the glass temperature have non-exponential time dependence; and non-Debye frequency responses⁹.

We consider other systems with structural transitions and equilibration delays. Martensitic steel alloys, when quenched from high temperature parent austenite to low temperature ‘martensite’^{10,11}, show strain domain-wall¹² patterns¹³⁻¹⁵. They can exhibit puzzling delays in conversion to martensite¹⁶⁻²⁰, that increase rapidly with temperature: raising T to nearer transition by a few percent, can raise delays from 1 sec to 10^4 seconds¹⁸.

We do Monte Carlo (MC) simulations of quenches in T , of martensitic discretized-strain²¹⁻²³ models in $3D$. The model hamiltonians describe the elastic Domain Walls (DW) or mobile twin boundaries, of four 3D structural transitions, each with characteristic anisotropic Compatibility interactions between order-parameter strains¹⁵. The four transitions²¹ can occur in martensite-related functional materials, where OP strains will be coupled to the functionality variables. The transitions are tetragonal-orthorhombic (YBCO, superconductivity); cubic-tetragonal (FePd, shape memory); cubic-orthorhombic (BaTiO, ferroelectrics); cubic trigonal (LaSrMnO, colossal magnetoresistance).

Our 3D simulations yield post-quench evolutions as in²⁴⁻²⁶ 2D, passing through three Domain Wall (DW) states. At first there is a majority-austenite DW Vapour state of a martensite droplet in an austenite background. This converts to majority-martensite DW Liquid, of randomly wandering walls. Finally the DW Liquid orders to a DW Crystal microstructure, with the walls along preferred directions¹³, as in parallel ‘twins’.

We focus on the conversion delays of the first evolution of DW Vapour \rightarrow DW Liquid, that corresponds to austenite to martensite conversions, or a rise of the martensite fraction $n_m(t)$ from zero to unity. As in the earlier 2D case²⁴⁻²⁶, a phase diagram in material parameters is obtained. In the ‘athermal’ martensite regime, there are curious ‘incubations’, or no apparent changes after a quench, terminated by sudden avalanche conversions¹⁶⁻²⁰. In this regime, we find three character-

istic temperatures, with $T_1 < T_d < T_0$. Here T_0 is the meanfield transition to uniform ordering.

Avalanche conversions in a single MC time step $t_m = 1$, occur for $T < T_1$, identified as the martensite start temperature^{10,11} $M_s = T_1$. Quenches into $T_1 < T < T_d$ show (postponed) avalanches²⁷ or *incubation* behaviour: the conversion fraction $n_m(t)$ remains flat at zero, until there is a jump up to unity a time $t = t_m(T)$. The incubation delay time $t_m(T)$ extends rapidly, on approaching a divergence temperature T_d . The physical picture for delays is of Vapour-droplet Fourier profile attempting entry to a negative-energy region of effective Hamiltonian spectra $\epsilon(\vec{k}, T) < 0$. The profile has to pass through a zero-energy \vec{k} -space contour at a bottleneck, like a Golf Hole edge²⁸⁻³¹. This transit passage delay differs from the familiar critical slowing down from a divergent Order Parameter length. The T -dependent, anisotropic bottleneck shrinks on warming, with a topological shape change at T_d , that blocks entry, so entropy barriers diverge. The precursor^{14,15} region $T_d < T < T_0$, where 2D results suggest dynamic tweed²⁷, may be studied elsewhere.

We use generic equilibration scenario of Ritort and colleagues to analyze the statistics^{1-4,31}, of the set of energy changes $\{\delta E\}$ from each MC step (usually used but not retained³²). These heat releases are recorded only up to an aging time $t_w = t_m(T)$, so the effective temperature depends on the quench temperature, $T_{eff}(t_w) \rightarrow T_{eff}(T)$: non-stationary distributions become time independent. We confirm the signature PES exponential tail for all four transitions. We find the search temperature vanishes linearly $T_{eff}(T) \sim T_d - T$, driving an entropy barrier divergence at T_d . The martensite-conversion times are thus predicted to show glass-like VFT behaviour, $e^{1/T_{eff}(T)} \sim e^{1/(T_d - T)}$ here understood as an arrest of PES cooling. Such VFT behaviour, is extracted from simulation and experimental¹⁶⁻¹⁸ data.

The plan of the paper is as follows. In Section II, we discuss the generic Partial Equilibration Scenario and our specific case of quenching across a phase transition. Section III describes for the four transitions in 3D, the discrete-strain clock-like spins and their T -dependent Hamiltonians. In Section IV we describe the MC simulations, with delay results from the phase space bottlenecks in Section V. Section VI shows that PES signatures are seen in all four transitions. Section VII shows that both 3D simulations and metallic alloy experiments exhibit VFT behaviour. Finally Section VIII is a summary.

Appendix A illustrates how a continuum double-well Landau free energy induces a T -dependent, Ising effective Hamiltonian. Appendix B obtains the athermal phase diagram for four transitions. Movies of post-quench DW evolutions are in Supplementary Material Videos²⁷.

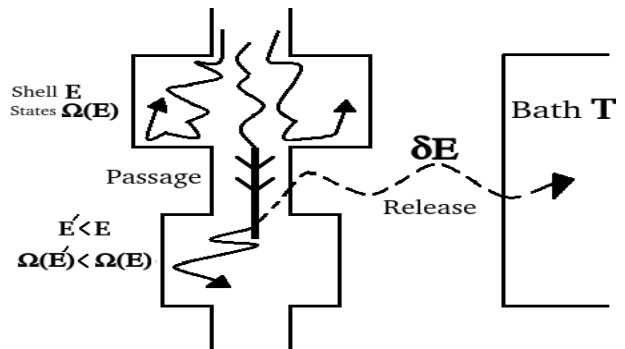


FIG. 1. *Schematic of Partial Equilibration Scenario* : The system in a configurational shell of states with energy E , states $\Omega(E)$, and entropy $S(E) = \ln \Omega(E)$ makes a passage to the next shell of lower $E' < E$, fewer states $\Omega(E') < \Omega(E)$ and smaller entropy $S(E') < S(E)$, crossing a generic entropy barrier to find rarer states. The turned-back wiggly lines are failed searches for passage. The downward bold line denotes successful searches, accompanied by a distribution of heat releases $\delta E \equiv E' - E < 0$ to the bath at T , scaled in an effective search temperature T_{eff} . Our case of quenches below a first-order transition can have further, specific entropy barriers, eg hindering system passage through order parameter-related, T -dependent, bottlenecks in phase-space.

II. SCENARIO FOR POST-QUENCH EQUILIBRATION:

How do systems re-equilibrate, after a temperature quench? Ritort and coworkers have suggested that if an equilibrium canonical ensemble in thermal contact with a heat bath suddenly has its bath quenched to a lower temperature T , then the system goes into an ageing ensemble¹⁻⁴, that has a quasi-microcanonical description of states of the system. There are sequential passages through decreasing-energy configurational shells, and intervening entropy barriers in the system-search for the new equilibrium. While delays from energy barriers are from attempts through activated jumps, to cross mountains, delays from entropy barriers are from attempts through constant-energy searches, to find rare channels going through or around, the mountain³¹.

In this Section we i) outline (our understanding of) the generic Partial Equilibration Ensemble¹⁻⁴ or PES, and ii) state how this ageing scenario is applied to our specific case, that has quenches across phase transitions, and order parameter emergence from zero.

i) Generic PES for ageing after quenches:

The PES for the equilibration process considers a system of energy E in contact with a (larger) heat bath. A familiar textbook derivation³³ of the canonical ensemble, applies the microcanonical ensemble to the system plus heat bath, of constant total energy $E_{tot} = E + E_{bath}$. The total number of states is the product of the $\Omega(E)$ states of the system, and of the $\Omega_{bath}(E_{tot} - E)$ states of the bath,

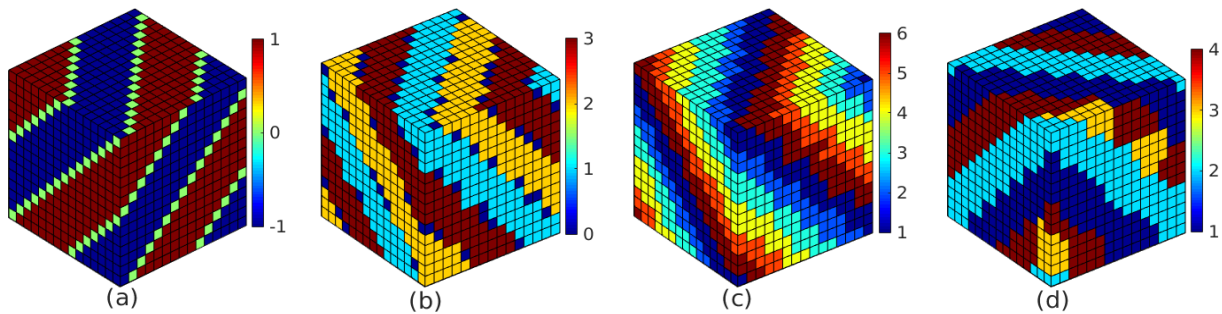


FIG. 2. *Microstructures in ferroelastic transition*: The Domain Wall crystal or twinned textures are shown, with variant label V in the colour bar. The Hamiltonian energy scale in is $E_0 = 3$, with the non-OP compressional constant $A_1 = 4$ fixing all other non-OP elastic constants, see text. The DW textures are (a) tetragonal-orthorhombic transition at $T = 0.45$ and Landau spinodal temperature $T_c = 0.95$; (b) cubic-tetragonal transition at $T = 0.4$ and $T_c = 0.95$; (c) cubic-orthorhombic transition at $T = 0.3$ and $T_c = 0.95$; and (d) cubic-trigonal transition at $T = 0.37$ and $T_c = 0.97$. Note that for each transition, all allowed variants are actually present.

summed over all allowed system energies $0 < E < E_{tot}$:

$$\Omega_{tot}(E_{tot}) = \sum_E \Omega(E)\Omega_{bath}(E_{tot} - E). \quad (1)$$

The system configurational entropy is $S(E) = \ln \Omega(E)$, and the inverse effective temperature is $\beta_{eff} \equiv 1/T_{eff} = dS(E)/dE$. Similarly, the inverse bath temperature is $\beta_{bath} \equiv 1/T_{bath} = dS_{bath}/dE_{bath}$. The change in total entropy depends on the system energy change dE as

$$dS_{tot} = \frac{dS(E)}{dE}dE + \frac{dS_{bath}}{dE_{bath}}dE_{bath} = [\beta_{eff} - \beta_{bath}]dE \geq 0 \quad (2)$$

with the equality at equilibrium, when the system and bath temperatures are equal $\beta_{eff} = \beta_{bath}$. The Second Law inequality $dS_{tot} > 0$ must hold, for the irreversible cases. After a bath quench from initial to a final $T_{bath} = T$, the system is left hotter, $T_{eff} > T$, or $\beta_{eff} - \beta < 0$. The energy changes are negative $dE = dQ < 0$, with heat released *by* the system *to* the bath.

At equilibrium, the terms in the sum of Equ (1) are dominated by clusters of energy shells selected³³ by a sharp peak, arising from the product of a rising number of system states $\Omega(E)$, and a falling bath factor $e^{-E/T_{bath}}$. The peak width is the energy fluctuations from stochastic system-bath exchanges. These equilibrium ideas describe *states*, not *processes*.

The Partial Equilibration Scenario postulates a plausible post-quench non-equilibrium *process* for the system to evolve between the initial and the final equilibrium state. A sudden change in bath temperature or quench, will induce a *shifted* peak, around a different equilibrium state. The post-quench system, initially stranded in non-optimum states, is visualized as moving through the sequentially lower energy shells of Equ (1) in its search for the shifted peak, tracked by an ageing time t_w .

The Scenario postulates that the system i) rapidly spreads ergodically through all states of a shell of energy E , and ii) slowly dribbles out energy $\{\delta E\}$ to the

ever-present energy bath. Since the system is partially equilibrated in the quasi-microcanonical shell, the equilibrium definitions can be retained, of the shell entropy $S(E)$ and its energy derivative $1/T_{eff}(t_w)$. The back-and-forth energy exchanges to rapidly surmount internal energy barriers and explore all shell configurations, are summoned by the system from the bath ('stimulated'). The slow changes on passages to a lower-energy shell, are releases by the system to the bath ('spontaneous').

Fig 1 is a schematic of the Partial Equilibration Scenario. The successive shells have lower energy $E' < E$ and hence lower number of configurations $\Omega(E') < \Omega(E)$ and entropies $S(E') < S(E)$. There is a generic *entropy* barrier $S_B \equiv -\Delta S = -\ln[\Omega(E')/\Omega(E)] > 0$ to finding the rarer states. Key seeks lock: most attempts fail.

From an ageing Fluctuation Relation³ the nonequilibrium energy-change probability¹⁻⁴ is a peak at the origin, times an exponential tail for negative changes. This generic PES signature tail depends on the ageing time through the the effective temperature $T_{eff}(t_w)$, that scales the heat releases:

$$P_0(\delta E; t_w) \simeq P^{(+)}_0(\delta E; t_w)e^{\delta E/2T_{eff}(t_w)}, \quad (3)$$

with an even prefactor $P^{(+)}_0(\delta E; t_w)$.

In an important result, other effective temperatures, from the Fluctuation-Dissipation Theorem; and from non-equilibrium fluctuations of system variables, are shown to be equal to the PES effective temperature¹: there is only one T_{eff} .

ii) *Specific PES from quenching across a transition.*

For our case of quenching to T across a first-order transition, the Order Parameter (OP) has to rise from zero, and so the wait times t_w to reach OP marker events will depend on the quench temperature, $t_w = t_m(T)$. The effective temperature and PES distribution will thus also depend on the quench temperature, $T_{eff}(t_w) \rightarrow T_{eff}(T)$ and $P_0(\delta E; t_w) \rightarrow P_0(\delta E, T)$. The even prefactor $P_0^{(+)}(\delta E, T)$ can be exponentiated and expanded to quadratic order, Equ (3) is then a gaussian peaked

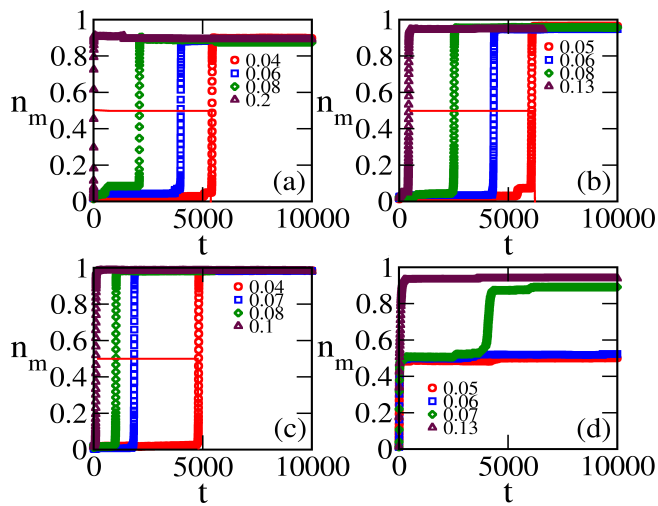


FIG. 3. *Conversion incubations ending in postponed avalanches:* Four-panel plot of martensite conversion fraction $n_m(t)$ versus time t , for fixed $E_0 = 3$, $A_1 = 4$ and different scaled temperatures $|\delta_0(T)| \equiv |T - T_d|/T_d$ as in the legend. There are flat incubations ending in explosive jumps in $n_m(t)$ at $t = t_m$ defined by $n_m(t_m) = 1/2$. (a) tetragonal-orthorhombic transition with Landau spinodal temperature $T_c = 0.9$; (b) cubic-tetragonal transition with $T_c = 0.95$; (c) cubic-orthorhombic transition with $T_c = 0.95$; (d) cubic-trigonal transition with $T_c = 0.97$, that is unusual, see text.

at the origin, times an exponential falloff. Completing the square yields a PES signature of a shifted gaussian, peaked at positive mean changes $M(T) = \langle \delta E \rangle$, and scaled in T_{eff} :

$$P_0(\delta E, T) \simeq e^{-[\delta E - M(T)]^2 / 4M(T)T_{eff}(T)}. \quad (4)$$

For small heat releases $\delta E = -|\delta E| < 0$, the PES distribution takes a Boltzmann-like form $P_0 \simeq e^{-\frac{1}{2}\beta_{eff}(T)|\delta E|}$. This gives a physical meaning to the effective temperature: it is a *search range* for accessible energy shells. If $\beta_{eff} \rightarrow 0$, entropy barriers collapse, and passages are immediate. If $T_{eff} \rightarrow 0$, then entropy barriers diverge, and passage-searches freeze.

We postulate that the OP-related bottlenecks can be of two types, depending on the depth of the quench. a) The DW Vapour \rightarrow Liquid delays are attributed to phase space bottlenecks²⁷, suggested by concepts in protein folding²⁸⁻³⁰. Hamiltonian energy-spectrum contours in Fourier space of zero energy are like a T -dependent Golf Hole (GH) edge, with a negative-energy Funnel region inside it leading to the final state²⁸. The entropic delays are from finding and entering the bottleneck.

b) For deeper quenches, the DW Liquid \rightarrow Crystal delays could be conceptually related to spin facilitation models^{27,34,35}, through the T -dependent sparseness of austenitic-hotspot dynamical catalysts, or other facilitating fields^{20,27}.

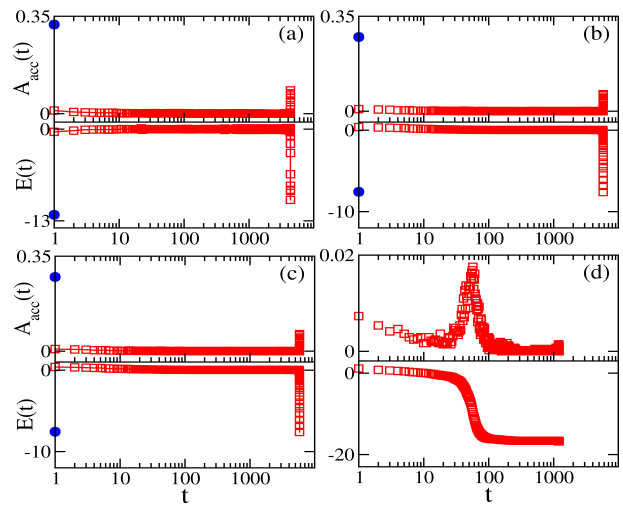


FIG. 4. *Acceptance spikes and energy drops:* Four-panel plots for all transitions, showing Acceptance fractions $A_{acc}(t)$ and total energies $E(t)$ versus time (displaced above and below the x -axis, for clarity). For $T < T_1$, eg for $\delta_0 = -0.7$, there are immediate spikes in $A_{acc}(t)$, and drops to negative values in energy $E(t)$, at the very first MC sweep $t = 1$ as denoted by on-axis blue solid circles. For $T > T_1$ eg for $\delta_0 = -0.1$, the red open squares show there are flat lines of incubation ending at $t = t_m$ postponed spikes and drops. The transitions a), b), c), d) are as in the Fig 3 Caption. Again, the cubic-trigonal case d) is unusual.

III. DOMAIN-WALL HAMILTONIANS FOR FOUR STRUCTURAL TRANSITIONS IN 3D:

The transition-specific, derived effective Hamiltonians have been presented in detail^{15,21-26}, and we just outline as conceptual background: A) Strains and Compatibility constraints. B) Reduction of continuum strains to discrete-strain ‘pseudo-spins’. C) Reduction of continuum strain free energies to effective ‘spin’ Hamiltonians.

It is useful to define N_{OP} the number of components of the OP strains; and N_V the number of Landau ‘variant’ minima at nonzero OP strain values. In terms of discretized strains, N_{OP} is the number of vector spin components, that can point in N_V variant directions. A double-well Landau free energy for a scalar magnetization maps onto (Appendix A) an Ising model with $N_{OP} = 1$ and $N_V = 2$. We consider four first-order transitions²¹ with $N_{OP} = 1, 2, 2, 3$. The nonzero, unit-magnitude variant vectors point respectively to corners of symmetry-dictated polyhedra with $N_V = 2, 3, 6, 4$ corners, inscribed in a unit circle or unit sphere: a geometrically pleasing sequence of line, triangle, hexagon, and tetrahedron. These transitions are respectively, tetragonal-orthorhombic, cubic-tetragonal, cubic-orthorhombic, and cubic-trigonal.

A. Strains and Compatibility:

Strains are symmetric tensors $\mathbf{e} = \mathbf{e}^T$, where the superscript T is Transpose. In three spatial dimensions, there are 6 independent Cartesian strains^{21,23} $e_{xx}, e_{yy}, e_{zz}, e_{xy}, e_{yz}, e_{zx}$. The *physical* strains $e_1, e_2 \dots e_6$ are convenient linear combinations: one compressional $e_1 = (e_{xx} + e_{yy} + e_{zz})/\sqrt{6}$; two deviatoric or rectangular $e_2 = (e_{xx} - e_{yy})/\sqrt{2}$, $e_3 = (2e_{zz} - e_{xx} - e_{yy})/\sqrt{6}$, and three shears $e_4 = e_{yz}, e_5 = e_{zx}, e_6 = e_{xy}$.

The free energy²¹ has a nonlinear Landau term that depends on a subset N_{OP} of these physical strains, as the Order Parameter(s). The remaining $n = 6 - N_{OP}$ non-Order Parameter physical strains enter the free energy as harmonic springs, whose extensions cannot be simply be set equal to zero, as pointed out by Kartha¹⁵. This is because a local OP-strained unit cell will generate non-OP strains in surrounding unit cells. To maintain lattice integrity all strained unit cells must mutually adapt, to all fit together in a *smoothly compatible* way, without dislocations.

For electromagnetism, there is a no-monopole Maxwell condition of vanishing divergence of the magnetic induction vector, $\nabla \cdot \vec{B} = 0$. For elasticity, there is a no-dislocation St Venant Compatibility condition of a vanishing double curl¹⁵, of the Cartesian strain tensor. In coordinate and Fourier space,

$$\nabla \times [\nabla \times \mathbf{e}(\vec{r})]^T = \vec{0}; \quad \vec{K}(\vec{k}) \times \mathbf{e}(\vec{k}) \times \vec{K}(\vec{k}) = \vec{0}. \quad (5)$$

Here $K_\mu(\vec{k}) \equiv 2 \sin(k_\mu a_0/2)$ for $\mu = x, y, z$, and lattice constant $a_0 = 1$. There are six differential-equation constraints, that are algebraic equations in Fourier space, of which only three are independent^{21,23}. Going to physical strains $e_1, e_2 \dots e_6$ the three $\vec{k} \neq 0$ algebraic equations express the non-OP strains in terms of the OP strains. The *uniform* $\vec{k} = 0$ non-OP strains are not so constrained, and can be freely set to their minimum value of zero.

The harmonic non-OP terms can then be analytically minimized subject to the $\vec{k} \neq 0$ linear constraints, by direct substitution for non-OP strains or by Lagrange multipliers. This yields an OP-OP effective interaction, with a transition-specific Compatibility Fourier kernel¹⁵ that depends on direction $\hat{k} \equiv \vec{k}/|\vec{k}|$. The kernels all have a prefactor $\nu_{\vec{k}} \equiv 1 - \delta_{\vec{k}, \vec{0}}$, that vanishes for $\vec{k} = \vec{0}$. The Compatibility kernels are smallest (eg zero) for specific directions \hat{k} , explaining the observed DW orientation along preferred crystallographic directions. The Compatibility potential in coordinate space is an anisotropic powerlaw, with the spatial dimensionality $d = 3$ as the fall-off exponent $\sim 1/R^d$.

B. Discrete-strain pseudo-spins:

The Landau free energy functionals $f_L(\vec{e})$ for a first order transition can be scaled to be independent or weakly

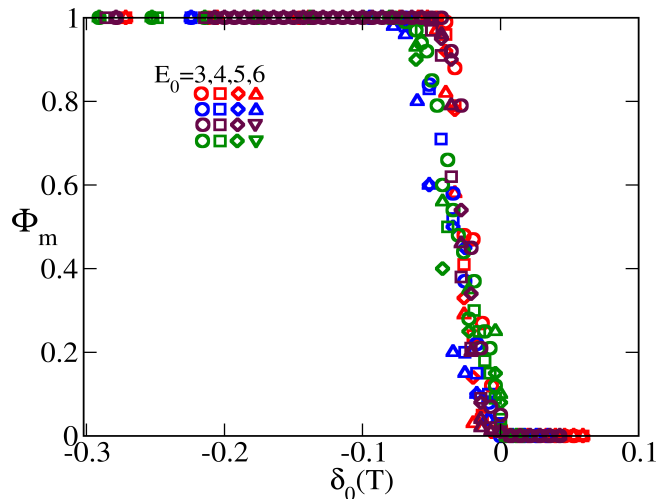


FIG. 5. *Conversion-success fraction*: The successfully converting fraction $\Phi_m(T)$ over 100 runs versus $\delta_0(T) \equiv (T - T_d)/T_d$ is shown in the range $T_1 < T < T_0$. The colours of symbols top to bottom denote transitions in order a) tetragonal-orthorhombic, b) cubic-tetragonal, c) cubic-orthorhombic, and d) cubic-trigonal. For a ‘precursor’ region $T_0 > T > T_d$, conversions do not occur. Success fractions are not exponentially sensitive to Hamiltonian energy scales $E_0 = 3, 4, 5, 6$, and are hence attributed to *entropy* barriers.

dependent, on material parameters²¹. With N_{OP} physical strains as a vector \vec{e} in OP space, the Landau free energy $f_L(\vec{e})$ in the austenite phase always has a turning point at $\vec{e} = \vec{0}$. In the martensite phase, it additionally develops N_V variant minima at $\vec{e} \neq 0$.

For first-order transitions, the scaled temperature is^{21–26},

$$\tau(T) \equiv (T - T_c)/(T_0 - T_c). \quad (6)$$

All energies are scaled in the thermodynamic Landau temperature where austenite and martensite free energies cross, so the scaled $T_0 = 1$. Here $T_c < T_0$ is the spinodal temperature where the austenite minimum vanishes, so uniform bulk austenite becomes unstable for $T < T_c$.

The local vector OP can be written as a product of magnitude and direction $\vec{e}(\vec{r}) = |\vec{e}(\vec{r})| \vec{S}(\vec{r})$. The N_V directions of variant or ‘spin’ vectors $\vec{S}(\vec{r})$ identify the degenerate variants on either side of a Domain Wall (DW), with all having unit magnitude, $\vec{S}(\vec{r})^2 = \sum_\ell S_\ell(\vec{r})^2 = 1$. Since austenite is always a Landau turning point, and in any case austenite could be induced at any T by local stresses, we always also include the austenite origin point $\vec{S}(\vec{r}) = \vec{0}$ as an allowed value^{21,22,24}.

The strain magnitudes are flat, deep into domains on either side of narrow Domain Walls that are zeros of the OP. The local strain magnitude is set equal to the uniform Landau mean value²¹, $|\vec{e}(\vec{r})| \simeq \bar{e}(T) > 0$, so components $\ell = 1, 2 \dots N_V$ are approximated as

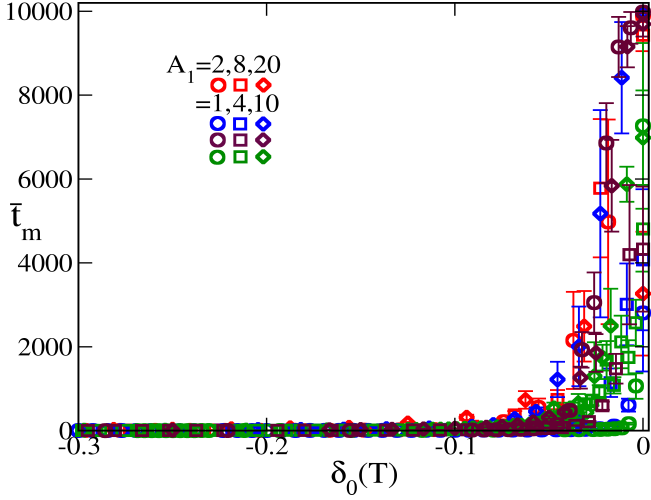


FIG. 6. *Delay times versus quench temperature*: Linear-linear plots of mean conversion delay time \bar{t}_m versus scaled temperature $\delta_0(T) \equiv (T - T_d)/T_d$ for $E_0 = 3$, and various A_1 elastic constants for the four transitions. (The symbol colours top to bottom denote transitions in the same order as Fig 5.) On approaching T_d , there are increasing standard-deviation error bars, suggesting a broadening rate distribution.

$$e_\ell(\vec{r}) \rightarrow \bar{\varepsilon}(T)S_\ell(\vec{r}). \quad (7)$$

Substituting into the variational free energy density²¹ with Landau, Ginzburg, and Compatibility terms $f = f_L(\vec{e}) + f_G(\nabla\vec{e}) + f_C(\vec{e})$, generates a T -dependent effective spin Hamiltonian $H(\vec{S}, T)$, with the same three terms, inheriting material-specific parameters such as T_c, T_0, A_1 . Each of the discretized-strain clock-like Hamiltonians have been systematically derived²¹ from continuous-strain free energies. They are bilinear in the spins, and encode the crystal symmetries, strain nonlinearities, and Compatibility constraints.

The DW Hamiltonian, with E_0 an energy scale (in units of T_0), is

$$F = E_0 \sum_{\vec{r}} [f_L + f_G + f_C] \quad (8)$$

$$\rightarrow H(\vec{S}, T) = H_L(\vec{S}, T) + H_G(\nabla\vec{S}) + H_C(\vec{S}).$$

Notice H has an inherent separation of time scales, with the magnitude $\bar{\varepsilon}(T)$ responding immediately to quenches $T < T_0$ in a single time-step, while the more sluggish DW adjustments of $\vec{S}(\vec{r})$ can take hundreds or thousands of MC time-steps.

With $\vec{S}^6 = \vec{S}^4 = \vec{S}^2 = 0, 1$, the Landau term is

$$\sum_{\vec{r}} f_L(\vec{e}) \rightarrow \sum_{\vec{r}} f_L(\bar{\varepsilon}\vec{S}) = f_L(T) \sum_{\vec{r}} \vec{S}(\vec{r})^2. \quad (9)$$

The Landau free energy density is

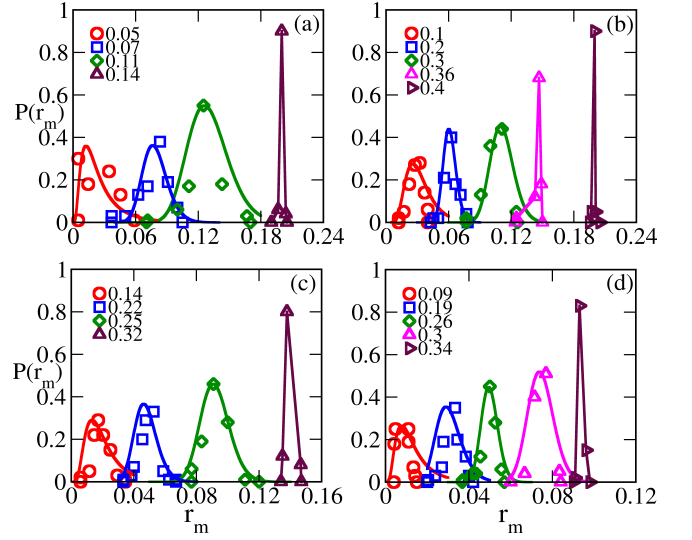


FIG. 7. *Distribution of conversion rates*: Four-panel plot of conversion rate distributions $P(r_m)$ versus rate r_m for $E_0 = 3, A_1 = 4$ and different $|\delta_0(T)|$ as in the legend. Log-normal distributions are shown as guides to the eye. Transitions are again in the order a) tetragonal-orthorhombic transition; b) cubic-tetragonal transition; c) cubic-orthorhombic transition; and d) cubic-trigonal transition. Fast processes are narrow, while slow processes are broad.

$$f_L(T) \equiv \bar{\varepsilon}(\tau)^2 g_L(T) \leq 0, \quad (10)$$

defining a factor $g_L(T)$, that vanishes at the Landau transition temperature $g_L(T_0) = 0$, and is negative below it.

For a *uniform* variant $\vec{S}(\vec{r}) = \vec{S}_0$ a constant vector, or in Fourier space $\vec{S}(\vec{k}) \sim \delta_{\vec{k},0}\vec{S}_0$, there is a vanishing of the Ginzburg term $\sim \vec{k}^2$, and of the Compatibility kernel $\sim \nu_{\vec{k}} = 1 - \delta_{\vec{k},0}$. The uniform (Landau) free energy then sets a lower bound to the energy, $H(\vec{S}, T) \geq N n_m(t) f_L(T) < 0$, where the martensite fraction is

$$n_m(t) \equiv (1/N) \sum_{\vec{r}} \vec{S}(\vec{r}, t)^2. \quad (11)$$

so $n_m = 1$ or 0 for uniform martensite or austenite.

As a 2D illustration²⁴⁻²⁶, the square-rectangle OP is a scalar, so $N_{OP} = 1$. There are two variants (rectangles along either x or y axes), so $N_V = 2$. The Landau free energy $f_L = e^2[(\tau - 1) + (e^2 - 1)^2]$ is a triple well in the OP strains. For $\tau = 1$, the three well depths at $e = 0, \pm 1$ are degenerate at zero. For $0 < \tau < 1$ the austenite well at $e = 0$ is metastable, and goes unstable at $\tau = 0$, the $T = T_c$ spinodal temperature. The Hamiltonian is diagonal in \vec{k} space, $\beta H = (D_0/2) \sum_{\vec{k}} [\epsilon(\vec{k}, T) |S(\vec{k})|^2]$, where $D_0 \equiv (2\bar{\varepsilon}^2 E_0/T)$. The energy spectrum for long wavelengths is $\epsilon(\vec{k}, T) = [-|g_L(T)| + \xi_0^2 k^2 + A_1 U(\hat{k})]$. The square-rectangle transition kernel depends on direction $\hat{k} = \vec{k}/|\vec{k}|$, or the single polar angle ϕ , as

$$U(\vec{k}) = \frac{\nu_{\vec{k}}(\hat{k}_x^2 - \hat{k}_y^2)^2}{[1 + (8A_1/A_3)\hat{k}_x^2\hat{k}_y^2]} = \frac{\nu_{\vec{k}}(\cos 2\phi)^2}{[1 + (2A_1/A_3)(\sin 2\phi)^2]} \quad (12)$$

where A_3/A_1 is the ratio of a non-OP (shear) elastic constant, and the non-OP compressional A_1 . The (positive) kernel has a maximum value $U(max) = 1$ at $\phi = \pm\pi/2$, and a minimum value $U(min) = 0$ at $\phi = \pm\pi/4$, driving a preferred DW orientation along both diagonals.

The energy spectrum for $A_1 = 0$ is a parabola pulled down to negative values by the Landau term, $\epsilon \sim [k^2 - |g_L(T)|]$. A zero energy contour in (k_x, k_y) space is a circle with a T-dependent radius $\sqrt{|g_L(T)|}$, that shrinks to a point at T_0 . For $A_1 \neq 0$, the bottleneck becomes angularly modulated, with a squared-radius $k^2(T, \phi) = |g_L(T)| - (A_1/2)U(\hat{k})$, interpolating between a $\phi = \pm\pi/4$ outer radius $k_{outer}^2(T) = |g_L(T)|$ and a $\phi = \pm\pi/2$ inner radius $k_{inner}^2(T) = |g_L(T)| - (A_1/2)$. The inner radius clearly vanishes at some temperature $|g_L(T_d)| = (A_1/2)$ where $T_d < T_0$. This characteristic temperature, from an interplay between Landau, Ginzburg, and Compatibility terms, is where the entropy barrier diverges.

Planes et al³⁶ consider a uniform-martensite model with a Landau variational term $f_L(e, T)$. Fast or slow behaviour is through first-passage-time jumps crossing an energy barrier, that collapses at T_c , or is largest at T_0 . Our spatially non-uniform martensite model with Ginzburg, Compatibility and Landau variational terms, differs in detail, but is similar in spirit. Fast or slow behaviour is through MC searches crossing an entropy barrier, that collapses at T_1 and diverges at T_d .

C. DW Hamiltonians for four transitions :

Clock models have discrete spins directed at N_V points on a unit circle, and are denoted by \mathbb{Z}_{N_V} , where the Ising model is \mathbb{Z}_2 . Here we generalize to include $\vec{S} = \vec{0}$, and call these ‘clock-zero’ models, denoted by \mathbb{Z}_{N_V+1} .

Drawing on Equ (7), the generic coordinate-space Hamiltonian is

$$\beta H = \frac{D_0}{2} [\sum_{\vec{r}} \sum_{\ell} \{g_L(T) \vec{S}_{\ell}(\vec{r})^2 + \xi_0^2 |\vec{\nabla} \vec{S}_{\ell}(\vec{r})|^2\} + \frac{A_1}{2} \sum_{\vec{r}, \vec{r}'} \sum_{\ell, \ell'} U_{\ell\ell'}(\vec{r} - \vec{r}') \vec{S}_{\ell}(\vec{r}) \vec{S}_{\ell'}(\vec{r}')] \quad (13)$$

where the overall energy scale is $D_0(T) \equiv 2\bar{\epsilon}^2(T)E_0/T$. Here ξ_0 is the domain-wall thickness parameter, A_1 is the elastic constant for the non-OP compressional strain²⁴⁻²⁶. The kernel $U_{\ell\ell'}$ is an $N_{OP} \times N_{OP}$ matrix potential, that carries the spatial dimensionality $d = 3$, and depends on ratios of other non-OP elastic constants to A_1 . Local meanfield treatments²² yield even the complex strain textures of some real materials^{13,14}.

The generic \vec{k} space Hamiltonian is obtained from $S_{\ell}(\vec{r}) = \frac{1}{\sqrt{N}} \sum_{\vec{k}} S_{\ell}(\vec{k}) e^{i\vec{k}\cdot\vec{r}}$, and as $\vec{S}(\vec{r})$ is real, $\vec{S}(\vec{k})^* =$

$\vec{S}(-\vec{k})$. The Hamiltonian and energy-spectrum are

$$\beta H = \frac{D_0}{2} \sum_{\vec{k}} \sum_{\ell, \ell'} \epsilon_{\ell\ell'}(\vec{k}, T) S_{\ell}(\vec{k}) S_{\ell'}(\vec{k})^*; \quad (14)$$

$$\epsilon_{\ell, \ell'}(\vec{k}, T) \equiv [\{g_L(T) + \xi_0^2 \vec{K}^2\} \delta_{\ell, \ell'} + \frac{A_1}{2} U_{\ell\ell'}(\vec{k})].$$

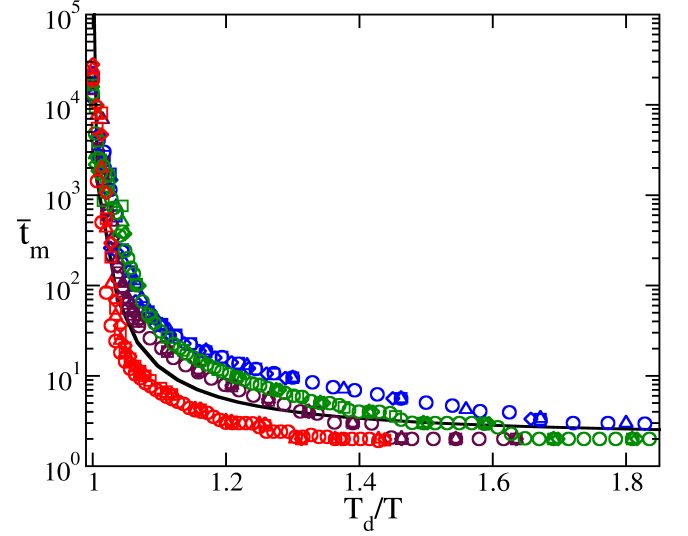


FIG. 8. Angell-type plot as in glasses, for athermal martensites: The delay times $\bar{\tau}_m(T)$ are replotted versus T_d/T , so that Arrhenius activated times would give a straight line. The x-axis data for the four transitions go from a value of unity on the left, to their respective T_d/T on the right. The obvious curvature shows that delays are not activated over energy barriers. They are attributed to *entropy* barriers.

The 3D transitions are given below in the sequence of $N_{OP} = 1, 2, 2, 3$, plus $N_V = 2, 3, 6, 4$ cases respectively.

a) *Tetragonal-Orthorhombic case* ($N_{OP} = 1, N_V = 2$): The scalar OP is the first deviatoric-strain OP $e_2 = (e_{xx} - e_{yy})/\sqrt{2}$, with \vec{S} having 2 + 1 values: at the origin, and pointing to the two endpoints of a unit-circle diameter. The Hamiltonian is like a 3D Spin-1 Blume Capel model²⁴, but with anisotropic power-law interactions, and with the quadratic term $f_L(T)\vec{S}^2$ where $f_L(T) < 0$. The Hamiltonian is a clock-zero \mathbb{Z}_{2+1} model²¹. The scalar compatibility kernel $U(\vec{k})$ for the tetragonal-orthorhombic transition is given in Equ. (A26) of Ref 21.

With $f_L(T) \equiv \bar{\epsilon}^2(T)g_L(T) \leq 0$, the Tetragonal-orthorhombic (and also 2D square-rectangle) case has the squared-mean OP and $g_L(T)$ factor as²¹

$$\bar{\epsilon}^2(T) = (2/3)[1 + \sqrt{(1 - 3\tau/4)}]; \quad (15)$$

$$g_L(T) \equiv (\tau - 1) + (\bar{\epsilon}^2 - 1)^2.$$

b) *Cubic-tetragonal case* ($N_{OP} = 2, N_V = 3$): This 3D transition has been considered earlier^{23,31}. The

OP strains are the two deviatoric strains $(e_3, e_2) = (\{2e_{zz} - e_{xx} - e_{yy}\}/\sqrt{6}, \{e_{xx} - e_{yy}\}/\sqrt{2})$. The spin values $\vec{S} = (S_3, S_2)$ vectors are in a plane in OP space, with \vec{S} having 3 + 1 values: at the origin and pointing to the three corners of a triangle inscribed in a unit circle. The Hamiltonian is a clock-zero \mathbb{Z}_{3+1} model²¹. The compatibility kernel is a 2×2 matrix, $U_{\ell\ell'}(\vec{k})$, with $\ell, \ell' = 2, 3$, as in Equ (A23) of Ref 21.

The mean OP and $g_L(T)$ of the cubic-tetragonal transition are

$$\begin{aligned} \bar{\varepsilon}(T) &= (3/4)[1 + \sqrt{(1 - 8\tau/9)}]; \\ g_L(T) &= (\tau - 1) + (\bar{\varepsilon} - 1)^2. \end{aligned} \quad (16)$$

c) *Cubic-orthorhombic case* ($N_{OP} = 2, N_V = 6$):

The OP strains are again the two deviatoric strains (e_3, e_2) as above. The nonzero $\vec{S} = (S_3, S_2)$ spin vectors are in a plane in OP space, with \vec{S} having 6 + 1 values: at the origin and pointing to the six corners of a hexagon inscribed in a unit circle. The Hamiltonian is a clock-zero \mathbb{Z}_{6+1} model²¹. The Compatibility kernel is a 2×2 matrix $U_{\ell, \ell'}(\vec{k})$, again with $\ell, \ell' = 2, 3$ and is the same as the cubic-tetragonal case, given in Equ (A23) of Ref 21.

The squared-mean OP and $g_L(T)$ for the Cubic-orthorhombic case, are the same as the tetragonal-orthorhombic in Equ (15).

d) *Cubic-trigonal case* ($N_{OP} = 3, N_V = 4$):

The three OP for the cubic-trigonal transition are the three shears $e_4, e_5, e_6 = e_{xy}, e_{yz}, e_{zx}$, and the variant vector has three vector components, with \vec{S} having 4 + 1 values: at the origin and pointing to the four corners of a tetrahedron inscribed in a unit sphere. The Compatibility kernel is now a 3×3 matrix $U_{\ell, \ell'}(\vec{k})$, with $\ell, \ell' = 4, 5, 6$, or six components $U_{44}, U_{55}, U_{66}, U_{45}, U_{54}, U_{64}$ as in Equ. (A20) of Ref 21.

The mean OP and $g_L(T)$ for the cubic-trigonal case are the same as the cubic-tetragonal case in Equ (16).

IV. MONTE CARLO SIMULATIONS:

Simulations were done on models for four transitions in 3D. The initial state $t = 0$ is 2% randomly and dilutely seeded martensite cells, in an austenite sea of $\vec{S} = 0$. Evolutions proceed at quench temperatures $T < T_0$. Typical parameters are $T_0 = 1$; $\xi_0^2 = 1$; $T_c = 0.81$ to 0.97 ; $A_1 = 1$ to 85 ; $E_0 = 3, 4, 5, 6$; $N = L^3 = 16^3$; $N_{runs} = 100$; and holding times $t_h = 10^4$ MC sweeps, each over N sites.

The Compatibility kernels arise from the non-OP harmonic terms, with $(6 - N_{OP})$ elastic constants. For all transitions, we specify the fixed ratio of other non-OP elastic constants, to A_1 . For the tetragonal-orthorhombic transition, with $N_{OP} = 1$ and S_2 as the OP spin, the non-OP elastic constants are the other deviatoric constant A_3 , and the three shear constants A_4, A_5, A_6 , set to be $A_3 = A_4 = A_5 = A_6 = A_1/2$. Similarly, for the cubic-tetragonal and cubic-orthorhombic cases with $N_{OP} = 2$

and (S_3, S_2) as the OP spins, the non-OP constants are set to be $A_4 = A_5 = A_6 = A_1/2$. Finally, for the cubic-trigonal case with $N_{OP} = 3$ and the shears (S_4, S_5, S_6) as the OP, the constants are set as $A_2 = A_3 = A_1/2$.

The standard MC procedure³² is followed, with an extra data retention¹⁻⁴ of energy changes.

0. Take N lattice sites, each with a vector spin of N_{OP} components, in one of $N_V + 1$ possible values (including zero) at MC time t . Each $\{\vec{S}(\vec{r})\}$ set is a ‘configuration’. With $n_m = 0$ or 1 for uniform austenite or martensite, the average martensite fraction is $n_m(t) \leq 1$. The conversion time t_m is defined as when²⁴ $n_m(t_m) = 1/2$.

1. Randomly pick one of N sites, and randomly flip the spin on it to a *new* direction/value, and find the (positive or negative) energy change δE .

2. If $\delta E \leq 0$, then accept the flip. If $\delta E > 0$, then accept flip with probability $e^{-\delta E/T}$. Record this spin-flip δE , that is usually not retained after use.

3. Repeat steps 1 and 2. Stop after N such spin-flips. This is the $t + 1$ configuration with $n_m(t + 1)$.

4. We collect all recorded $\{\delta E\}$ over each MC sweep of every run while tracking $n_m(t)$. The collection is only up to a waiting time equal to the martensite conversion time. $t = t_w \leq t_m(T) \leq t_h$. We do six quenches, from $T = T_1$ upwards to T_d .

A single-variant athermal martensite droplet or ‘embryo’¹¹ can form anywhere, and after a local conversion at a waiting time $t_w = t_m$, can *propagate* rapidly to the rest of the system^{11,19}. Hence it is the mean *rates* \bar{r}_m (or inverse times), that are averaged over N_{run} runs, analogous to total resistors in parallel determined by the smallest resistance. The mean times \bar{t}_m are defined as the inverse mean rates²⁴.

$$\bar{r}_m(T) = \frac{1}{N_{run}} \sum_{n=1}^{N_{run}} \frac{1}{t_m(n)}; \quad \bar{t}_m(T) \equiv \frac{1}{\bar{r}_m(T)}. \quad (17)$$

For an un-successful n -th run that does not convert in a holding time t_h , the rate $r_m(n)$ could be assigned a value of either $1/t_h$ (conversion right after cutoff) or 0 (conversion never occurs). We choose the $1/t_h$ cutoff, that shows up as a flattening of the mean rate near T_d . An extrapolation of the linear part of $r_m(T)$ to the temperature axis yields a value²⁴ for T_d .

V. DELAYS AND BOTTLENECKS:

For the four transitions, we consider i) Delays from sluggish Domain Walls; ii) Bottlenecks in Fourier space.

A. Delays from sluggish Domain Walls

Figure 2 shows the twinned microstructures in all four transitions, colour coded through the variant-label V , where $V = 0$ is always austenite. For the single-OP

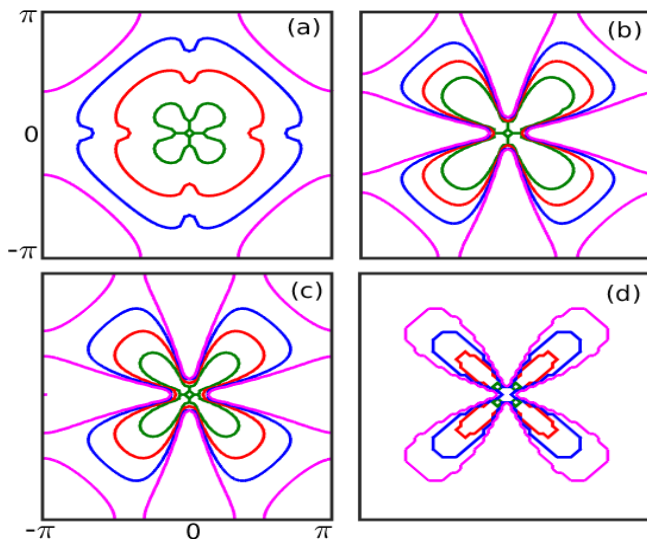


FIG. 9. *Bottlenecks in phase space for different transitions:* Four-panel plot shows energy contours on 2D slices of the 3D bottleneck, with $\delta_0(T) = -0.1, 0, +0.1, +0.2$. The sizes decrease on warming, and the bottleneck inner radius is seen to pinch off, at some T_d' . The contours are a) Tetragonal-orthorhombic, $T_d' = 0.69$ b) Cubic-tetragonal, $T_d' = 0.60$; c) Cubic-orthorhombic $T_d' = 0.60$; d) Cubic-trigonal $T_d' = 0.70$. The corresponding delay-divergence temperatures $T_d = 0.75, 0.59, 0.69, 0.75$ are close in value, and taken as the same, for simplicity of discussion.

tetragonal-orthorhombic transition, $V = \pm 1$ has two variant colours. For the two-component OP, the cubic-tetragonal and cubic-orthorhombic transitions have respectively, $V = 1, 2, 3$ and $V = 1, 2, \dots, 6$ variant colours. For the three-component OP, the cubic trigonal has $V = 1, 2, 3, 4$ four variant colours. Fig 2 shows that *all* allowed degenerate N_V variants are present, for all four transitions.

The tetragonal-orthorhombic, and cubic-tetragonal twins can have Domain Walls decorated with austenite, as also found in the 2D case²⁵. Such observed austenite retentions¹¹ can be understood: they are energetically favoured, when the lower Ginzburg costs of austenite-martensite walls compensate for the absence of the negative condensation energy $f_L(T) < 0$ of martensite unit cells. As T is lowered, the energy accounting is reversed, and the austenite inclusions are expelled, replaced by martensite, so DW are only between martensite variants²⁵.

We define a fractional deviation from a characteristic temperature T_d , as

$$\delta_0(T) \equiv (T - T_d)/T_d \leq 0. \quad (18)$$

Figure 3 shows the martensite conversion-fraction $n_m(t)$ versus MC time t in a *single run*, for different $\delta_0(T)$. For quenches to below $T = T_1$, there is an immediate avalanche conversion in a single $t = 1$ sweep, characteristic of athermal martensite. For temperatures

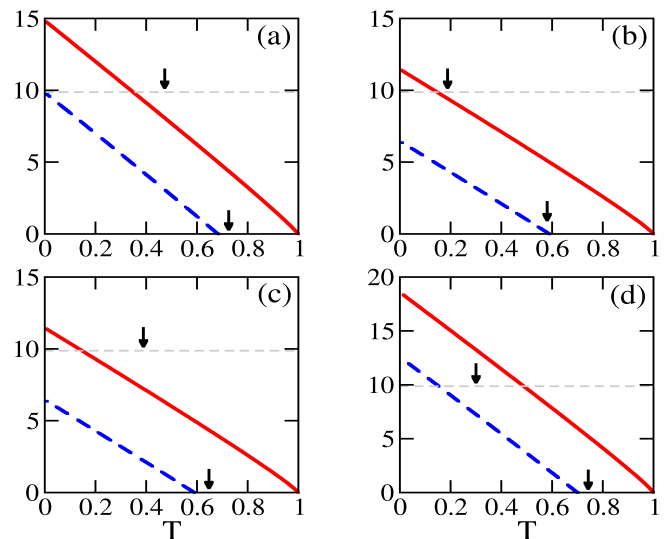


FIG. 10. *Bottleneck inner and outer radius:* Four-panel plot showing $k_{outer}^2(T)$ (solid), $k_{inner}^2(T)$ (dashed) lines versus temperature T , for transitions in the order a) to d) as in Fig 9. The inner radius vanishes close to the delay-divergence T_d (downward arrows). The outer radius vanishes at the thermodynamic transition temperature $T_0 = 1$. It intersects the horizontal light dashed line denoting a Brillouin Zone scale π^2 , at temperatures close to the $T_1 = 0.51, 0.21, 0.4, 0.31$ for explosive conversions (downward arrows)

$T > T_1$ there is a strange ‘incubation’ behaviour, or a postponement of these avalanches. The fraction $n_m(t)$ remains virtually unchanged, up till $t = t_m$ when $n_m(t)$ rises sharply through $1/2$, to unity. The cubic-trigonal transition has $N_{OP} = 3$ order parameter components, $N_V = 4$ variants, and can show unusual behaviour. Here, there is an initial jump to $n_m = 1/2$ followed by incubation, and then a jump to unity.

Fig 4 shows that for $T < T_1$ there is an immediate spike in the MC acceptance fraction $A_{acc}(t)$ at $t = 1$, and drop in energy $E(t)$ to negative values. For $T > T_1$, during incubations they both remain zero, up to $t = t_m(T)$, when the acceptance spikes and the energy drops. Again, the cubic-trigonal case is unusual.

What goes on microscopically, during incubation? In 2D, Video²⁷ A shows random initial seeds of both variants (red, blue) can quickly form an almost zero energy single-variant martensitic droplet or embryo (red) in an austenite background (green), in the DW Vapour state. The small droplet extends and retracts amoeba-like arms, searching for energy-lowering pathways. After a long conversion delay t_m of hundreds of time steps, when $n_m \simeq 0$, the single-variant droplet (red) suddenly expands rapidly and generates the opposite variant (blue). This is the wandering-wall or DW Liquid state. After a shorter orientation delay, the walls of the DW Liquid orient to a DW crystal.

Figure 5 shows for all four transitions, the mean fraction of successful conversions Φ_m during a holding time

$t = t_h$ over 100 runs, versus the temperature deviation $\delta_0(T)$. For temperatures $\delta_0 \leq -0.1$, every run converts, and $\Phi_m = 1$. However, for $\delta_0 > -0.1$, $\Phi_m(T)$ falls through 1/2 at $\delta_0(T) \sim -0.05$, and then to zero. The success fraction is not exponentially sensitive to overall energy scales $E_0 = 3, 4, 5, 6$, so the probability of conversion is not activated over an energy barrier.

Just above T_d there are unsuccessful runs (not shown), when the martensite seeds can dissolve back into austenite. The seeds will not be regenerated, even if the holding time t_h is increased, or if the temperature is lowered²⁰.

Figure 6 shows a linear-linear plot of the mean conversion times \bar{t}_m versus $\delta_0(T)$ for various E_0 . The absence of exponential sensitivity to E_0 implies the delays are not activated over energy barriers, but are due to *entropy barriers*. For $T < T_1$ fluctuations are small, while for $T > T_1$ standard-deviation error bars $\pm\sigma$ over the $N_{run} = 100$ runs, are larger, on approaching T_d .

If the probability of entropy-barrier crossings coming from a product of sequential random steps, a *logarithm* of rates would be an additive random variable, suggesting a log-normal distribution of rates²⁵ $P(r_m)$. Fig 7 shows optimized-bin histograms³⁷ of r_m data, with (asymmetric) log-normal lines as guides to the eye. Although data are too sparse to decide distributions, clearly fast conversions are narrow, and slow conversions are broad, similar to protein folding^{29,30}.

Fig 8 shows an Angell-type plot⁸ of log delay time versus $T_d/T > 1$. Arrhenius-type activations over energy barriers would be linear. The delays have curvatures, and so must be from entropy barriers. The solid curve is VFT behaviour of Equ (29) below, with $B_0 = 0.25$.

B. Bottlenecks in Fourier-space:

We draw on concepts of protein folding²⁸⁻³⁰, to understand the entropy barrier delays.

A purely random search of protein configurations could take astronomical times (Leventhal paradox). Rapid protein folding is attributed to a configuration-space Golf Hole (GH) opening into a Funnel of negative-energy configurations, leading rapidly to the folded protein state^{28,29}. Bicout and Szabo³⁰ consider a random walk of a Brownian particle in a space of eigen-labels of protein folding modes (that could be analogous to propagative martensitic twinning modes³⁸). The Brownian particle has to locate and enter spherical zero-energy GH contour of marginal modes. Unusual delays can occur, at the GH edge.

In our case, the bottleneck is fixed by the energy spectrum from Equ (14) in 3D Fourier space (taken as diagonal in ℓ , for discussion):

$$\epsilon_{\ell\ell}(\vec{k}, T) = \xi_0^2 \vec{K}(\vec{k})^2 - |g_L(\tau)| + (A_1/2)U_{\ell\ell}(\hat{k}). \quad (19)$$

Energy spectra set to a constant C or $\epsilon_{\ell\ell}(\vec{k}, T) = C$, define contours in \vec{k} -space. The Ginzburg term at long

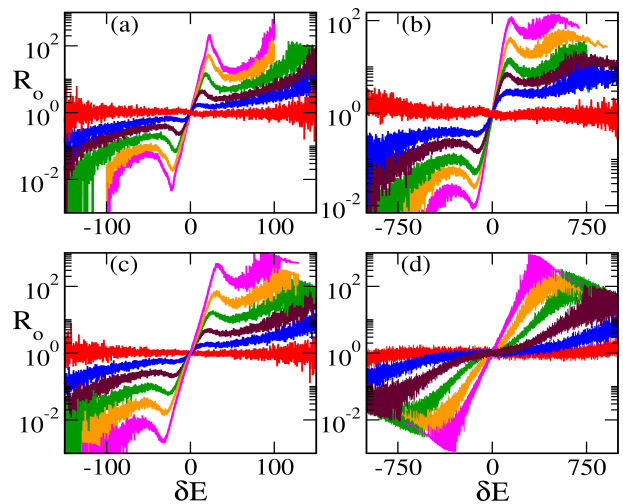


FIG. 11. Fluctuation ratios R_0 of forward/backward energy change probabilities in log-linear plot: Four-panel plot for all transitions, of the ratio $R_0(\delta E, T) \equiv P_0(\delta E, T)/P_0(-\delta E, T)$ versus MC energy change δE , for six T .

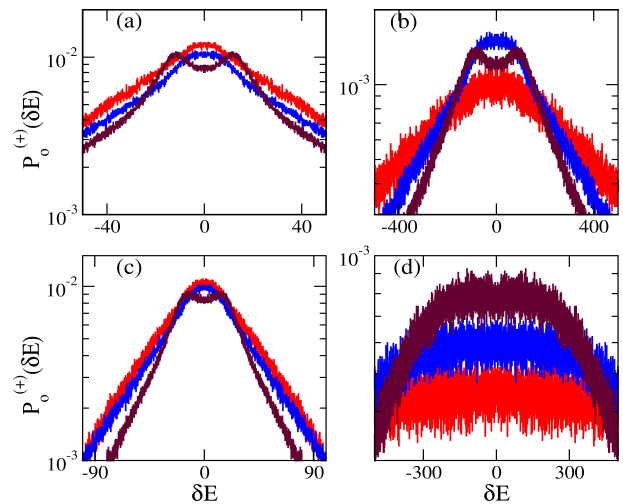


FIG. 12. Even-symmetry prefactor $P_0^{(+)}$ in linear-linear plot: Four-panel plot for all transitions, checking that the log-linear prefactor $P_0^{(+)}(\delta E, T)$ versus energy change δE has no linear contribution near the origin.

wavelengths $\sim \vec{k}^2$, forms a \vec{k} -space spherical bowl in 3D, with zero-energy minimum at the origin. The Compatibility term $U_{\ell\ell}(\vec{k})$ angularly modulates its 2D surface to produce an anisotropic zero-energy contour²⁴.

The phase-space boundary $\epsilon_{\ell\ell}(\vec{k}, T) = 0$ separates an outside \vec{k} region of positive (austenite) energies, from a \vec{k} -region inside, of (martensitic) negative energies. Video B shows²⁷ a 2D circular droplet Fourier profile in (k_x, k_y) as it distorts, to enter the phase space bottleneck.

We consider spectra with $\epsilon_{22}(\vec{k}, T)$ for the first three transitions, and $\epsilon_{66}(\vec{k}, T)$ for the cubic-trigonal case.

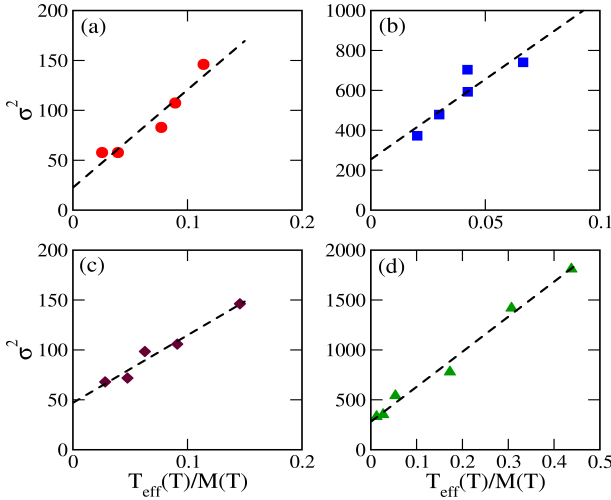


FIG. 13. *Variance of the even-symmetry prefactor* : Four-panel linear-linear plot of the variance $\sigma^2(T)$, of the prefactor $P_0^{(+)}(\delta E, T)$, versus $T_{eff}(T)/M(T)$ for the four transitions. The energy scale is chosen as the (positive) mean energy change $M(T) \equiv \langle \delta E \rangle$ over the entire PES distribution.

Consistent with the twin orientations in Fig 1, the plane intersecting the 3D bottleneck to yield a 2D cross-section is taken as $[\hat{k}_x, \hat{k}_y, \hat{k}_z] = [1, 1, 1]$. The plane through the Brillouin Zone origin is $k_x + k_y + k_z = 0$, and Fig 9 shows for all four transitions, the T -dependent contours of constant $\epsilon_{\ell\ell}(k_x, k_y, k_z = -k_x - k_y, T)$ versus (k_x, k_y) for temperature range $\delta_0(T) = -0.1$ to $+0.2$. As mentioned, the cubic-tetragonal and cubic-orthorhombic have the same kernel but different Landau factor $g_L(T)$, so one would expect the second and third panels to show the same overall shapes, but slightly different energy contours for a given T : this is indeed the case.

The bottleneck sizes are large at low T and small at high T . The contours are angularly modulated between a smaller inner-radius wave-vector $k_{inner}(T)$ and larger outer-radius wave-vector $k_{outer}(T)$. From the spectrum Equ (19)

$$\begin{aligned} k_{outer}^2(T) &= \xi_0^{-2} [|g_L(T)| - (A_1/2)U_{\ell\ell}(min)]; \\ k_{inner}^2(T) &= \xi_0^{-2} [|g_L(T)| - (A_1/2)U_{\ell\ell}(max)]. \end{aligned} \quad (20)$$

For $U_{\ell\ell}(min) = 0$, the outer square-radius vanishes at the Landau temperature, $k_{outer}^2(T_0) = |g_L(T_0)| = 0$. Close to transition,

$$k_{outer}^2(T) \simeq b(T_0)(T - T_0) \quad (21)$$

where the Taylor expansion coefficient $b(T) \equiv -dg_L(T)/dT < 0$.

With a positive $U_{\ell\ell}(max) > 0$ there is a temperature $T_d < T_0$ where the inner radius can pinch off to zero, $k_{inner}^2(T_d) = |g_L(T_d)| - (A_1/2)U_{\ell\ell}(max) = 0$, while the outer radius is still nonzero. Near T_d ,

$$k_{inner}^2(T) = |g_L(T)| - |g_L(T_d)| \simeq b(T_d)(T - T_d). \quad (22)$$

Figure 10 shows the inner and outer squared-radii, both almost linear, and vanishing respectively at T_d and T_0 .

The conversion-delay divergence comes from a pinch-off of the inner radius $k_{inner}(T)$ of the bottleneck. The topology of a 2D slice of the 3D negative energy states, goes from an open butterfly to a segmented four-petalled flower²⁵. It is impossible for the broad Fourier profile of a small droplet to distort at zero total energy, into four separated petal-like segments. The lower-energy states for $T > T_d$ are thus available, but not accessible. The inter-shell configurational pathway closes; the success-fraction vanishes; and the entropy barrier diverges.

VI. PES SIGNATURES IN ALL FOUR TRANSITIONS

We now exhibit PES signatures in the four athermal martensite transitions. Entropy barriers are insensitive to energy scales, so we consider only $E_0 = 3$.

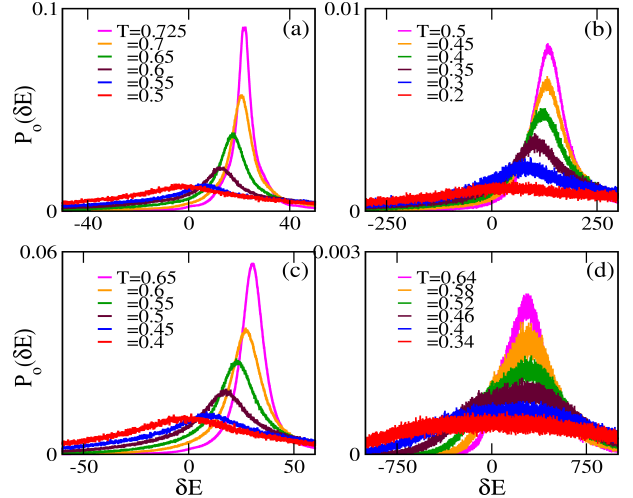


FIG. 14. *Normalized probabilities P_0 of energy-changes in linear-linear plot*: Four-panel Figure for all transitions, showing the probability $P_0(\delta E, T)$ versus energy change δE for the six quench temperatures T in the legend. The probabilities are consistent with the predicted PES signature of shifted Gaussians peaked near a mean energy changes $M(T) > 0$, with exponential heat-loss tails for $\delta E < 0$.

As noted the MC procedures of Section IV retain the set of *single spin-flip* energy changes $\{\delta E\}$ from all N spin-flips, in each of N_{run} runs, up to t MC times $t \leq t_m(T)$. The histograms can be dense since the data set size can be large: $N \times t_m \times N_{run}$ has up to $16^3 \times 10^4 \times 100$ data points.

An ageing-state fluctuation relation is postulated⁴. The probability $P_0(\delta E, T)$ to hit configurations E' from

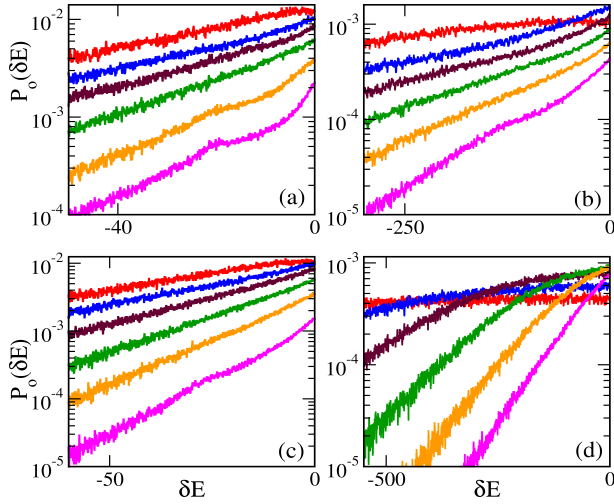


FIG. 15. *Normalized probability of energy-changes P_0 in log-linear plot* : Four-panel Figure for all transitions, showing a log-linear version of Fig 14 on a zoomed in scale of $P_0(\delta E, T)$ versus energy change δE , at the same six temperatures T . The linear behaviour is a PES signature, with slopes determining the inverse effective temperatures, $\beta_{eff}/2 \equiv 1/2T_{eff}$, that flatten near $T = T_1$.

E , is proportional to the *target size*, or the number of accessible states: $P_0(\delta E, T) \sim \Omega(E')$, with $S(E') = \ln \Omega(E')$, where $E' = E + \delta E < E$. The reverse path has $P_0(-\delta E, T) \sim \Omega(E)$. The ratio of forward and backward probabilities $R_0(\delta E)$ is related to the entropy change and entropy barrier $\Delta S(\delta E) \equiv S(E') - S(E) \equiv -S_B < 0$. Thus

$$R_0 \equiv \frac{P_0(\delta E, T)}{P_0(-\delta E, T)} = \frac{\Omega(E')}{\Omega(E)} = e^{\Delta S(\delta E)}. \quad (23)$$

Fig 11 shows four-panel log-linear plots of the fluctuation ratio $R_0(\delta E, T)$. Since $R_0(\delta E)R_0(-\delta E) \equiv 1$, the entropy change is odd, $\Delta S(\delta E) + \Delta S(-\delta E) = 0$, and a solution is

$$P_0(\delta E, T) = P_0^{(+)}(\delta E, T) e^{\frac{1}{2}\Delta S(\delta E)}, \quad (24)$$

where the (even) prefactor is the geometric mean, $P_0^{(+)}(\delta E, T) = \sqrt{P_0(\delta E, T)P_0(-\delta E, T)}$. For small energy changes, $S(E + \delta E) - S(E) \simeq \beta_{eff}\delta E$, and hence $P_0(\delta E, T) \simeq P_0^{(+)}(0, T) e^{\frac{1}{2}\beta_{eff}(T)\delta E}$.

Fig 12 is just a check that the prefactor $P_0^{(+)}(\delta E, T)$ versus δE has no linear contribution near the origin, that might modify the exponential tail. For temperatures near T_1 it is a single-peak gaussian, while near T_d it can go bimodal.

Fig 13 shows that the variance σ^2 of the weight $P_0^{(+)}(\delta E, T)$ versus a scaled $T_{eff}(T)$ is linear and non-singular, for all four transitions.

Fig 14 shows four-panel linear-linear plots of (normalized) $P_0(\delta E, T)$ versus δE for four transitions, each at one of six temperatures in the Legend. The peak is at positive energy as in the oscillator case², and moves left as T decreases towards T_1 . The exponential tails near the origin are barely visible.

Fig 15 shows the same four plots but now in log-linear form, and zoomed in. The curves all show the PES signature of linearity around the origin $\delta E = 0$. The cubic tetragonal panel has been shown earlier³¹. As T is lowered to T_1 , the slopes $\beta_{eff}(T)/2$ all flatten.

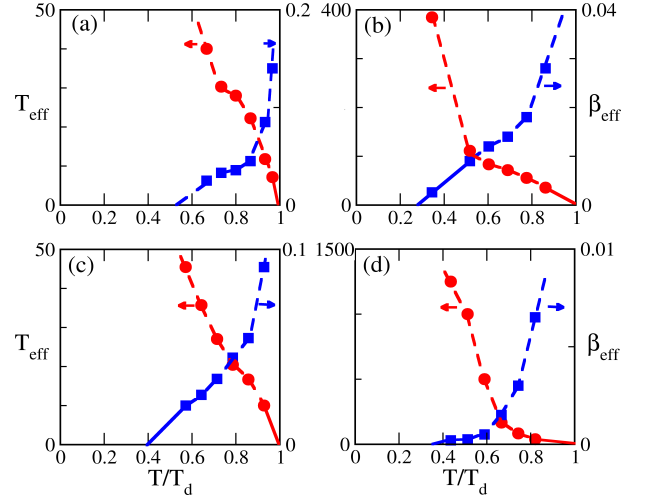


FIG. 16. *Effective temperature (and its inverse) versus quench temperature*: Four-panel Figure for all transitions, showing effective search temperature on the left vertical axis versus T . For all transitions, the T_{eff} vanishes linearly $\sim T_d - T$ at a search-freezing temperature T_d . The inverse $\beta_{eff}(T)$ on the right vertical axis vanishes linearly $\sim T - T_1$ at a search explosion temperature T_1 .

Fig 16 shows a central result, namely the search temperature $T_{eff}(T)$ and its inverse, $\beta_{eff}(T)$ versus T . The left-axis search temperature $T_{eff}(T)$ intersects the temperature axis at an extrapolated $T_{eff}(T_d) = 0$, defining a quench temperature T_d . The vanishing appears to be linear, $T_{eff}(T) \sim T_d - T$.

The mean conversion rate involves an integral over the heat releases of the distribution³⁹. The mean time is then a singular exponential $\bar{t}_m \simeq t_0 e^{M/4T_{eff}} \simeq t_0 e^{B_0 T_d / (T_d - T)}$. The Vogel Fulcher-Tammann form^{5,7,8} thus emerges naturally from a search temperature freezing inducing a rapid arrest of PES cooling, and an entropy-barrier divergence.

Similarly, the inverse effective temperature $\beta_{eff}(T)$ on the right-axis of Fig 16 seems to go to zero linearly $\sim (T - T_1)$ at a search explosion T_1 where entropy barriers vanish.

Once again, the cubic-trigonal last panel is unusual, with T_{eff} showing a smaller slope near T_d . If the linear slope actually vanishes as $T_{eff}(T) \sim (T - T_d)^2$ then that would yield ‘super-VFT’ behaviour⁵, $t_m \sim e^{1/(T - T_d)^2}$.

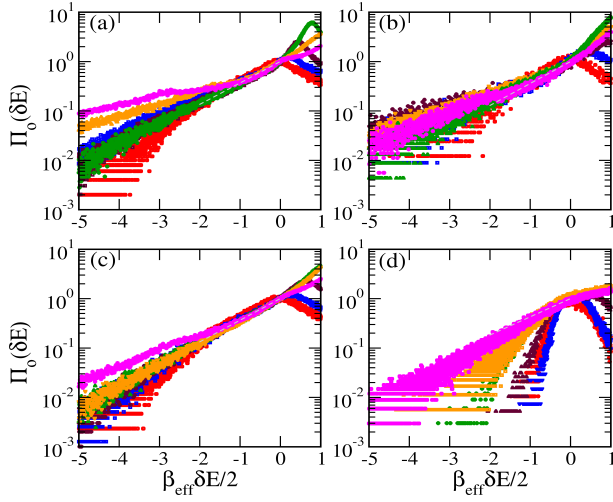


FIG. 17. Four panel plot of scaled probability of energy change Π_0 versus $z = \beta_{eff}\delta E/2$. The four transitions in panels a),b),c),d) have respective slope mean values and standard deviations of 1.000 ± 0.045 ; 1.025 ± 0.036 ; 1.009 ± 0.08 ; 0.850 ± 0.085 .

Fig 17 shows the scaled ratio of occurrence probability to its value at the origin, $\Pi_0 \equiv P_0(\delta E, T)/P_0(0, T)$ versus $z \equiv \beta_{eff}\delta E/2 \simeq \delta S/2$. The dashed white lines have slopes close to the predicted universal slope of unity, as given in the Figure caption.

The normalized probability P_{MC} of a Monte Carlo spin-flip is the product of the occurrence probability P_0 and an MC acceptance factor with step functions,

$$P_{MC}(\delta E, T) = \frac{P_0(\delta E, T)}{N_{MC}(T)} [\theta(-\delta E) + e^{-\delta E/T} \theta(\delta E)], \quad (25)$$

with $N_{MC}(T)$ a normalization constant. The ratio of the MC probability and its value at the origin defines $\Pi_{MC}(\delta E, T) \equiv [P_{MC}(\delta E, T)/P_{MC}(0, T)]$. With $z \equiv \beta_{eff}(T)\delta E/2$,

$$\Pi_{MC} \simeq [e^z \theta(-\delta E) + e^{-z(2T_{eff}/T)-1} \theta(\delta E)]/N_{MC}(T). \quad (26)$$

Fig 18 shows a log-linear plot of Π_{MC} along the positive axis $z = \beta_{eff}\delta E/2 > 0$. The closeness of data to theoretical lines with slope $[1 - 2T_{eff}/T] < 0$ is further evidence for PES.

In conclusion all four transitions show PES signatures, lending support to the Partial Equilibration Scenario.

VII. PES DELAYS IN SIMULATIONS AND EXPERIMENT

We show that delay data both in simulations and in experiment, are consistent with a picture of diverging en-

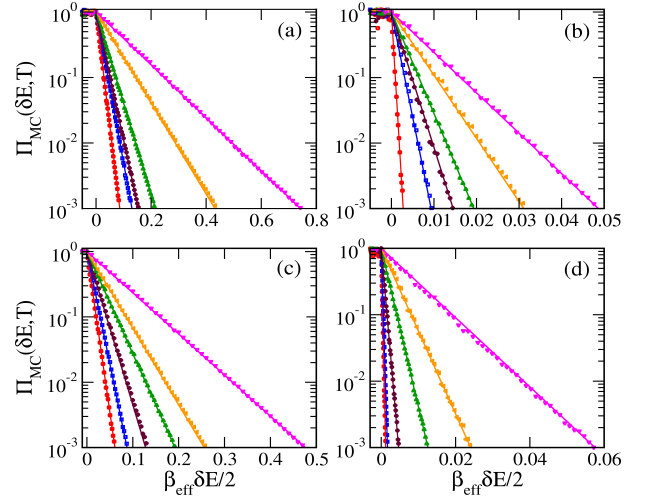


FIG. 18. Four panel plot of Π_{MC} versus $z = \beta_{eff}\delta E/2 > 0$. The light theoretical line of slope $[1 - 2T_{eff}/T]$ has a reasonable match to data.

ergy barriers from linearly vanishing PES effective temperatures.

A. VFT delays in 3D simulations

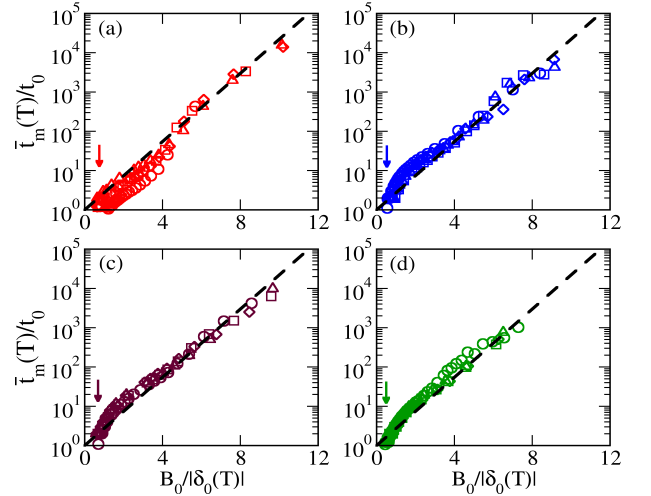


FIG. 19. Vogel-Fulcher-like behaviour in simulations: Four-panel plot of scaled data in simulations of log-linear scaled \bar{t}_m/t_0 versus scaled $B_0/|\delta_0(T)|$, for the four transitions a),b),c), d), with each panel showing $E_0 = 3, 4, 5, 6$. Data clustering for small $|\delta_0(T)|$, on the dashed line over three orders of magnitude is evidence for Vogel-Fulcher behaviour. For lower temperatures, there is a peel-off towards the x-axis near $T = T_1$ (downward arrow).

Vogel-Fulcher-Tamman temperature dependences can

be written near T_d as

$$\bar{t}_m(T) = t_0 e^{B_0 T_d / |T - T_d|} = t_0 e^{B_0 / |\delta_0(T)|} \quad (27)$$

where $t_0, B_0 T_d$ are the time and energy scales, for DW shifts of a lattice spacing.

The logarithms of VFT times can be written in two useful forms, to extract constants B_0, t_0 from simulations and experiments. Thus

$$\frac{1}{\ln \bar{t}_m(T)} = \frac{(|\delta_0(T)|/B_0)}{[1 + (\log t_0)(|\delta_0(T)|/B_0)]} \quad (28)$$

and

$$\ln \bar{t}_m(T) = \log t_0 + [B_0 / |\delta_0(T_0)|]. \quad (29)$$

For simulations, B_0 and t_0 can be extracted from data using Equ (28) and Equ (29). Fig 19 shows for all four transitions, the data in a scaled form of

$$\ln(\bar{t}_m/t_0) = B_0 / |\delta_0(T)|. \quad (30)$$

There is data clustering around the Vogel-Fulcher straight line showing universality over 3 orders of magnitude near T_d . There is also a peel-off toward shorter times, near T_1 (downward arrow).

B. VFT delays in martensitic alloys

Delayed athermal martensitic transformations in metallic alloys have been tracked by conversion diagnostics suited to the scale of the waiting times^{16–18} such as electrical resistivity drops; or surface optical or X-ray reflectivity. In pioneering experiments, Kakeshita et al¹⁷ used resistivity drops to detect the austenite to martensite delayed conversions for alloys $Fe_x Ni_{1-x}$. The alloying percentage $100x$ is 29.9, 31.6, 32.1%, with start temperatures of $M_s = 239, 177, 148$ K. The delays discovered were of macroscopically long times. Other work such as the Klemradt group^{16,18} on $NiAl$ alloy delays, also rose rapidly: for temperature increments above the M_s values of 0.1 K, 0.6 K and 0.7K, the delay times went from¹⁸ several seconds, to 10^4 seconds, to forever.

The data analysis of simulations is used again for experiment, as now described in more detail. To extract divergence temperatures T_d from simulation or experimental data, we plot $1/\ln(t)$ versus T , and extrapolate²⁴ straight line segments to the x-axis (not shown). For FeNi data¹⁷ this yields $T_d \simeq 247, 187, 158$ K, well above M_s , with large fractional delay windows $|\delta_0(M_s)| = |T_d - M_s|/T_d = 0.03, 0.05, 0.06$. Similarly extrapolation of data for the NiAl alloy¹⁸ with $M_s = 282.2$ K yields $T_d = 283$ K but with a smaller window $|\delta_0(M_s)| \simeq 3 \times 10^{-3}$.

Another group considered NiTi alloys²⁰, and argued that if the largest delay is at $T = T_0$, then for a long

enough annealing time, conversions should be seen at any T in a wide window $M_s < T < T_0$. However no conversion was detected, for holding at $T = 275.9$ above $M_s = 274.3$ K, for $t_h = 21$ days. The absence of conversion was attributed to a sparseness of (atomic) catalyst fields in facilitation-type delay models²⁰. In our picture this absence could also be due to T being outside the narrower conversion window $M_s < T < T_d < T_0$,

Fig 20 shows measurement data of conversion times t , in seconds, versus temperature T in degrees Kelvin. The left column shows a linear-linear plot like Equ (28) of $1/\ln t$ versus $|\delta_0(T)|$ to extract slope $1/B_0$ from Kakeshita data¹⁷ for three alloys of FeNi (top panel); and from Klemradt data¹⁸ for a NiAl alloy (bottom panel). The right column shows a linear-linear plot Equ (29) of $\ln t$ versus $1/|\delta_0(T)|$, using lines of the extracted slope B_0 , to determine the intercept $\ln t_0$ for FeNi (top panel) and for NiAl (bottom panel). Downward arrow marks $T_1 =$ for NiAl data. The ‘fragility’⁸ parameter $B_0 T_d = 1.23$ K, and a basic time scale for DW hops is $t_0 = 1$ second.

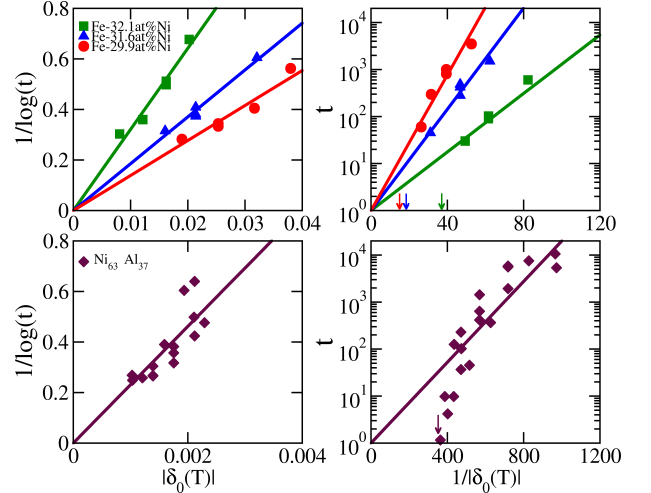


FIG. 20. *Vogel-Fulcher-like behaviour in experiment*: Left column shows data from both groups^{16–18}, in a $1/\ln(t)$ versus $|\delta_0(T)|$ plot. The slope $1/B_0$ is extracted from a fit to $y = (1/B_0)x$. Right column again shows results of both groups, in a log-linear plot of $\ln \bar{t}_m$ versus $1/|\delta_0(T)|$. The NiAl data show a downward deviation towards $T = M_s$ marked by the downward arrow. Using the extracted B_0 values, the intercepts are found in a fit to $y = B_0 x + y_0$.

Fig 21 shows that combined experimental data^{16–18} cluster around the Vogel-Fulcher straight line of Equ (30), with universality over 3 orders of magnitude near T_d . For NiAl data¹⁸, there is a linear falloff on approaching T_1 (downward arrow), consistent with Fig 16.

It would be interesting to get more data for these and other martensitic alloys, through systematic quenches in steps of $1/|\delta_0(T)|$, over the entire delay range $M_s < T < T_d$ between barrier divergence and collapse. It would also be interesting to include a T_1 -like onset of sluggishness, in fitting analyses of glass-former viscosity data⁷

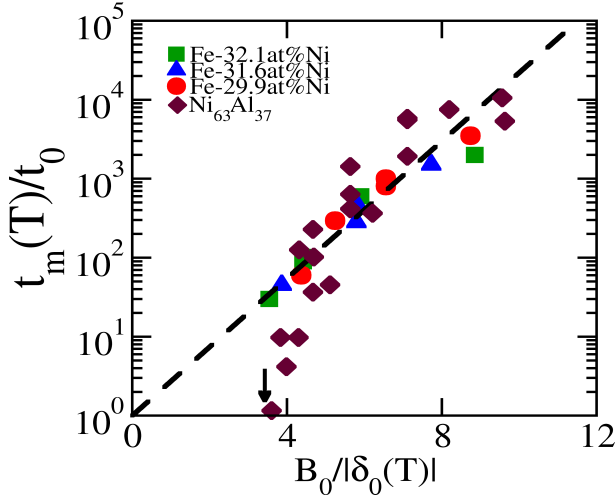


FIG. 21. *Entropy barrier collapse and divergence in scaled variables, for experiment:* Combined data from experiments in linear-linear plot of $\log(t/t_0)$ versus $B/|\delta_0(T)|$. The dashed straight line is the universal Vogel-Fulcher-Tammann form of the diverging entropy barrier. Some data show a downward turn for entropy barrier collapse.

VIII. SUMMARY AND FURTHER WORK

In this paper, we present Monte Carlo (MC) simulations, on discrete-strain Hamiltonians for four 3D structural transitions, under systematic temperature quenches from seeded austenite, to study austenite-to-martensite conversion times. The results and scenario are as follows.

For athermal martensites, there are explosive conversions below a martensite start temperature M_s so there are no barriers. Above this start temperature, entropy barriers emerge, and incubation time delays rise sharply towards a divergence temperature T_d . The entropy barrier collapse/divergence, is understood through temperature-controlled phase-space bottlenecks.

Partial equilibration ideas provide an understanding of fast/slow times, based on effective temperatures for energy-lowering searches. The inverse search temperature vanishes linearly at M_s or $1/T_{eff}(T) \sim |T - M_s| \rightarrow 0$. The search temperature vanishes linearly at T_d , or $T_{eff}(T) \sim |T - T_d| \rightarrow 0$. This rapid search arrest explains the singular Vogel-Fulcher-Tammann form, extracted from martensitic experimental data.

Further simulations of crystallisation models⁶ could try to record heat releases. Further experiments could record strain signals and intermittency⁴⁰ over the delay region $T_d > T > T_1$; and over the tweed precursor^{14,25,27} region above it $T_0 > T > T_d$. Non-stationary distributions of energy changes in martensites could be measured through concurrent acoustic, photonic or strain probes⁴⁰. The VFT temperature regime in glasses shows non-Debye frequency responses⁹: this might be more general. Finally, quenches of complex oxides⁴¹ near their structural / functional transitions, might

yield interesting PES signatures in functional variables, induced by their coupling to ageing strain domains.

Acknowledgements:

It is a pleasure to thank Turab Lookman for helpful early conversations; and Smarajit Karmakar for valuable discussions on the glass transition.

Appendix A: PES signatures in the m^4 model:

As a toy model illustration of the Section III procedure we consider a 2D magnetization free energy with double-well Landau term and a Ginzburg term, $F = E_0 \sum_{\vec{r}} [f_L + f_G]$, Here m is the single component OP, of both signs, so $N_{OP} = 1, N_V = 2$. The Landau term is

$$f_L(m(\vec{r})) = \epsilon(T)m(\vec{r})^2 + m(\vec{r})^4/2 \quad (31)$$

where $\epsilon(T) \equiv (T - T_c)/T_c$, with all energies/ temperatures scaled in the physical transition temperature, so the scaled $T_c = 1$. The Ginzburg term is $f_G = \xi_0^2 [\Delta m(\vec{r})^2]$.

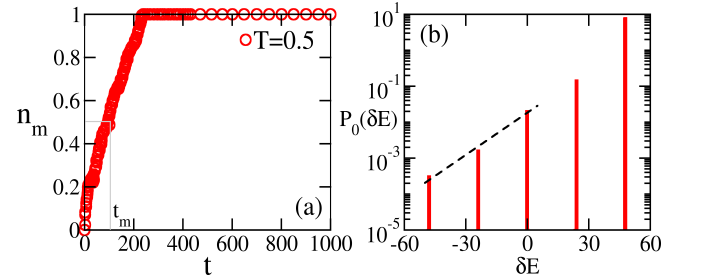


FIG. 22. *Magnetization fraction and PES distribution:* a) Linear-linear plot of magnetization fraction $n_m(t)$ versus time after a quench to $T = 0.5$. The curve at $n_m(t_m) = 1/2$ defines a halfway time $t_m(T)$, that here is $t_m = 107$ MC steps. b) Log-linear histogram of normalized probability of heat release $P_0(\delta E, T)$ versus δE after the quench, recording energy changes up to waiting times $t_w = t_m(T)$. Here the slope is $\beta_{eff}/2 = 0.09$, or $T_{eff} = 5.6$.

Domain-walls are solitonic solutions with a tanh profile, interpolating between flat OP variants of opposite sign, within a DW thickness $\xi_0 \sim 1$. The OP can be written as a magnitude $|m|$ times a variant ‘spin’ $S(\vec{r}) = \pm 1$ of unit length. The nearly flat magnitude in the domains is approximated by the mean field OP,

$$m(\vec{r}) \equiv |m(\vec{r})|S(\vec{r}) \rightarrow \bar{m}(T)S(\vec{r}) \quad (32)$$

where $\bar{m}(T) = |\epsilon(T)|^{1/2}$. Compare Equ (7).

The mean-field Landau free energy is

$$f_L(T) = \bar{m}(T)^2 g_L(T); \quad g_L = -\frac{1}{2}|\epsilon(T)| < 0. \quad (33)$$

where $g_L(T_c) = 0$. Compare Equ (10).

Substituting Equ (32) in Equ (31) yields the DW coordinate space Hamiltonian, with $D_0 \equiv 2\tilde{m}^2 E_0/T$,

$$\beta H = (D_0/2) \sum_{\vec{r}} [-|g_L(T)|S(\vec{r})^2 + \xi_0^2(\Delta S(\vec{r}))^2], \quad (34)$$

although in this case, $S(\vec{r})^2 = 1$ at all sites. With $S(\vec{r}) = \sum_{\vec{k}} e^{i\vec{k}\cdot\vec{r}} S(\vec{k})/\sqrt{N}$, the Hamiltonian in Fourier space is

$$\beta H = (D_0/2) \sum_{\vec{k}} [-|g_L(T)| + \xi_0^2 \vec{K}(\vec{k})^2] |S(\vec{k})|^2. \quad (35)$$

Compare Equ (13) and Equ (14).

We can do MC simulations with this T-dependent, Ising-variant effective Hamiltonian. The parameters are $N = 64^2$, $\xi_0^2 = 1$, $N_{run} = 10$, with holding times $t_h = 10^3$. The spin-flips are $S = \pm 1 \rightarrow \mp 1$. Fig 22a shows the magnetization fraction $n_m(t)$ versus waiting time t_w analogous to Fig 3, but here with a gradual rise, and no incubation behaviour.

We record $\{\delta E\}$ for every spin flip up to an OP marker event time $t_w = t_m$ when $n_m(t_m) = 1/2$. For nearest-neighbour couplings on a square lattice, the energy changes δE will be discrete. Fig 22b shows the log-linear $P_0(\delta E, t_w = t_m)$ versus discrete energy changes δE . The spike heights decrease linearly with energy changes, consistent with PES. Compare Fig 15.

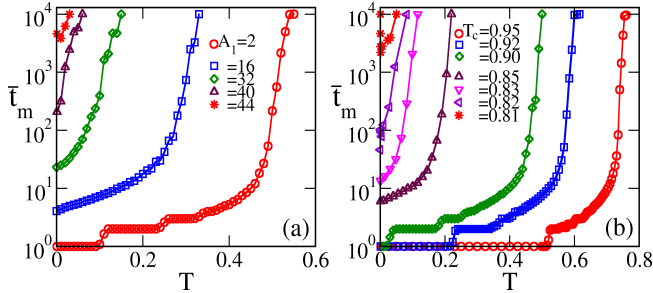


FIG. 23. Tetragonal-orthorhombic TTT curve, showing both explosive and incubated conversions: Figures show TTT curves as log-linear plots of time versus quench temperature. Flat regions along the x-axis denote single time-step conversions up to end points $T = T_1$, defining athermal regime materials. The T_1 depend on the elastic constants A_1 and spinodal temperatures T_c . For some parameters, T_1 is driven to zero, and the TTT curves intersect the y-axis. These materials are in a ‘mixed’ regime. See text.

Appendix B: Athermal phase diagram:

Fig 23 shows data for the martensitic tetragonal-orthorhombic transition, for several T_c, A_1 , showing both athermal and non-athermal or mixed behaviour^{11,23–25}. For the athermal regime, Temperature-Time-Transformation (TTT) curves have flat lines along the temperature axis where there are immediate, explosive conversions for $T < T_1$. The embryo or droplet is

small in coordinate space, and so is broad and flat in

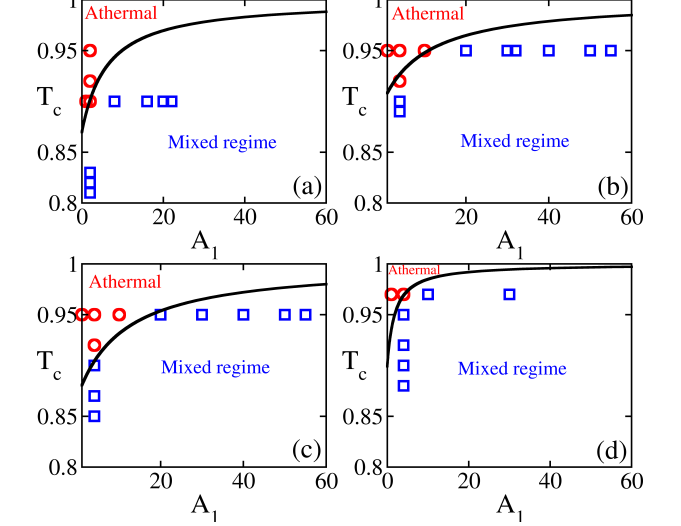


FIG. 24. Phase diagrams for athermal/ mixed behaviour: Four-panel Figure showing linear-linear plots of T_c versus A_1 solid line the theoretical boundary between athermal and mixed materials. Simulation data for athermal (open circles) and mixed (open squares) behaviour, are consistent with the theoretical curve.

Fourier space. With $|\vec{S}(\vec{k})|^2$ approximated by a constant, the Hamiltonian energy of Equ (18) is $E/D_0 \sim \sum_{\vec{k}} \epsilon(\vec{k})$ then involves averages of terms over the Brillouin Zone, denoted by square brackets. The droplet energy is

$$E(T)/D_0 \simeq -|g_L(T)| + \{\xi_0^2 [K^2(\vec{k})] + (A_1/2)[U_{\ell,\ell}(\hat{k})]\}. \quad (36)$$

The energy vanishing $E(T_1) = 0$ defines $T = T_1$. For small values in a Taylor expansion, and with coefficient $b(T)$ as defined in the text,

$$T_1(A_1, T_c) \simeq \{+|g_L(0)| - \xi_0^2 [K^2(\vec{k})] - (A_1/2)[U_{\ell,\ell}(\hat{k})]\}/|b(0)|. \quad (37)$$

We define ‘athermal’ behaviour as a nonzero T_1 ; explosive conversions for $T < T_1$; and incubation delays in the window $T_1 < T < T_d < T_0$. The behaviour not precisely athermal, is called ‘mixed’, with conversions occurring gradually, without flat incubations. Vanishing of the athermal case start temperature $T_1(A_1, T_c) = 0$ then determines a phase boundary.

The four-panel Fig 24 plot of T_c versus A_1 , shows the phase boundary. Above the phase boundary the system is purely athermal, while below the phase boundary where $T_1 = 0$, is a mixed regime. Data from Fig 23 and other TTT diagrams are seen to be consistent with the theoretical phase boundary. Fig 23 shows that for some parameters, curves on the upper left, have a fall and then a rise with temperature, like a ‘U shape, or downward ‘nose’. For the large $E_0 = 3$ used, the shape is distorted, but for smaller $E_0 < 1$ the U shape is more well defined²⁶. The shape is from an Arrhenius activation over a temperature-dependent energy barrier⁴².

- ¹ F. Ritort in *Unifying Concepts in Granular Media and Glasses*, (eds.) A. Coniglio, A. Fierro, H.J. Herrmann and M. Nicodemi, Elsevier B.V. (2004); arXiv/ condmat/ 03113710, v1.
- ² L. L. Bonilla, F.G. Padilla and F. Ritort, *Physica A* **250**, 315 (1998);
F. Ritort, *J. Phys. Chem. B* **108**, 6893 (2004);
L. Garriga and F. Ritort, *Phys. Rev. E* **72**, 031505 (2005).
- ³ A. Crisanti and F. Ritort, *Europhys. Lett.* **66**,253 (2004);
L. Buisson, L. Bellon and S. Ciliberto, *J. Phys. C*, **15**, S1163 (2003).
- ⁴ A. Crisanti, M. Picco and F. Ritort, *Phys. Rev. Lett.* **110**, 080601 (2013).
- ⁵ K. Binder, W. Kob, *Glassy Materials and Disordered Solids: An Introduction to Their Statistical Mechanics*, World Scientific, Singapore (2005).
- ⁶ H. Fang, M.F. Hagan, W.B. Rogers, *Proc. Nat. Acad. Sci.*, **117**, 27927 (2020);
X- Yang, H. Tong, W-H. Wang, and K. Chen, *Phys Rev E*, **99**, 062610 (2019);
H- Shintani and H. Tanaka, *Nature Physics* **2**, 200 (2006).
- ⁷ P. Lunkenheimer, S. Kastner, M. Koehler and A. Loidl, *Phys. Rev. E* **81**,051504 (2011).
- ⁸ *Fragility of glass-forming liquids* ed. A.L. Greer, K.F. Kelton, S. Sastry, Hindustan Book Agency, New Delhi (2014).
- ⁹ R. Boehmer, K.L. Ngai, C.A. Angell, D.J. Plazek, *J. Chem. Phys.*, **99**, 4201 (1993); T.V. Ramakrishnan and M. Rajalakshmi, Eds. *Non-Debye Relaxation in Condensed Matter*, World Scientific, Singapore (1987).
- ¹⁰ K. Bhattacharya, *Microstructure of Martensite*, Oxford University Press (2003),
EKH Salje, *Phase Transitions in Ferroelastic and elasto-Elastic Crystals* Cambridge (1993).
- ¹¹ J.R.C. Guimaraes and P.R. Rios, *J. Mater. Sci.*,**43**, 5206 (2008);
M. Rao and S. Sengupta, *Current Science (Bangalore)* **77**, 382 (1999);
Physical properties of martensite and bainite: Proceedings of the joint conference, the British Iron and Steel Research Association and the Iron and Steel Institute, Special report **93**, London (1965);
A. R. Entwistle, *Metall. Trans.* **2**, 2395 (1971);
SR Pati and M Cohen, *Acta Metall.*, **17**, 189 (1960);
G.V. Kurdjumov and O.P. Maximova, *Doklad. Akad. Nauk USSR* **61**, 83 (1948); **73**, 95 (1950).
- ¹² G.R. Barsch and J.A. Krumhansl, *Phys. Rev. Lett.* **53**, 1069 (1984).
- ¹³ J.W. Seo and D. Schryvers, *Acta Mater.*, **46**, 1165 (1998);
C. Manolikas and S. Amelinckx, *Phys. Stat. Sol. A* **61**,179 (1980).
- ¹⁴ L.E. Tanner, *Phil. Mag* **14**,111 (1966).
- ¹⁵ S. Kartha, J. A. Krumhansl, J. P. Sethna, and L. K. Wickham, *Phys. Rev. B* **52**, 803 (1995);
M. Baus and R. Lovett, *Phys. Rev. A* **44**, 1211 (1991);
S.R. Shenoy, T. Lookman, A. Saxena and A.R. Bishop, *Phys. Rev. B* **60**, R12537 (1999).
- ¹⁶ L. Müller, U. Klemradt, T.R. Finlayson, *Mat. Sci. and Eng. A* **438**, 122 (2006).
- ¹⁷ T. Kakeshita, T. Fukuda and T. Saburi, *Scripta Mat.* **34**, 1 (1996).
T. Kakeshita, K. Kuroiwa, K. Shimizu, T. Ikeda, A. Yamagishi, and M. Date, *Materials Transactions, JIM*, **34**, 423 (1993).
- ¹⁸ M. Aspelmeyer, U Klemradt, L.T. Wood and S.C. Moss, *Phys. Stat. Sol. (a)* **174**, R9 (1999);
U. Klemradt, M.Aspelmeyer, H. Abe, L.T. Wood, S.C. Moss and E. Dimasi, *J.Peisl, Mat. Res. Soc. Symp. Proc.* **580**, 293 (2000);
L. Mueller, M. Waldorf, C. Gutt, G. Gruebel, A. Madsen, T.R. Finlayson, and U. Klemradt, *Phys. Rev. Lett.* **107**, 105701 (2011).
- ¹⁹ P.R. Rios and J.R.C. Guimaraes, *Scripta Mat.*, **57**, 1105 (2007);
P.R. Rios, F.G. Cardoso, T.A. Neves, J.R.C. Guimaraes, in *The Minerals, Metals and Materials Society (eds) TMS 2015 144th Annual Meeting and Exhibition*, Springer, Cham (2015),
https://doi.org/10.1007/978-3-319-48127-2_84.
- ²⁰ K. Otsuka, X. Ren and T. Takeda, *Scripta Mat.* **45**,145 (2001).
K. Otsuka and X. Ren, *Scripta Mater.*, **50**, 207 (20004);
T. Okuzuno, Y. Yamazaki and T. Ohta, *Phys. Rev. B*, **67**, 654106 (2005).
- ²¹ S.R. Shenoy, T. Lookman and A. Saxena, *Phys. Rev. B* **82**, 144103 (2010).
- ²² R. Vasseur , T. Lookman and S. R. Shenoy, *Phys. Rev. B* **82**, 094118 (2010).
- ²³ K.O. Rasmussen, T. Lookman, A. Saxena, A.R. Bishop, R.C. Albers and S.R. Shenoy, *Phys. Rev. Lett.* **87** (2001);
SR Shenoy, T Lookman and A Saxena in *Magnetism and structure in functional materials*,Eds. A Planes and A Saxena Springer-Verlag, Berlin (2005).
- ²⁴ N. Shankaraiah, K. P. N. Murthy, T. Lookman and S. R. Shenoy, *Europhys. Lett.* **92**, 36002 (2010).
- ²⁵ N. Shankaraiah, K.P.N. Murthy, T. Lookman and S.R. Shenoy, *J. of Alloys Comps* **577**, S66 (2013);
Phys. Rev. B **84**, 064119 (2011);
Phys Rev. B **91**, 214108 (2015).
- ²⁶ N. Shankaraiah, *Phys. Rev. E* **95**, 063003 (2017); *J. Alloys Comps.* **675**, 211 (2016).
- ²⁷ Videos for the 2D square-rectangle $N_{OP} = 1, N_V = 2$ transition, with austenite (green) and the two martensite variants (red/ blue), show^{24,25} sequentially evolving Domain Wall phases, from DW Vapour to DW Liquid to DW Crystal or oriented ‘twins’. The 3D evolution is similar, but we present the earlier^{24,25} 2D system 64² as illustrations.
Video A. The droplet in \vec{r} -space: This shows the coordinate-space evolution for $T_d > T > T_1$, for the Golf Hole type constrained passage of Fig 1. Random initial martensite seeds rapidly form a single-variant DW Vapour droplet. The droplet fluctuates while slowly searching for a conversion passage to a bidiagonal DW Liquid. There is then a quick symmetry-breaking to single-diagonal DW crystal.
Video B. The droplet in \vec{k} -space: This shows for $T_d > T > T_1$, the evolution as in Video A but now in Fourier space. Videos C,D are in different quench regimes than A,B but are also given for completeness.
Video C. The \vec{r} -space dynamic catalysts: This shows the evolution for deep quenches $T \ll T_1$, of the facilitation type constrained passage. The DW Vapour now converts rapidly to a DW Liquid of sluggish walls. Sparse transient

hotspots of austenite in martensite act as dynamic catalysts, that non-locally delete even far-off minority-diagonal DW segments, leaving a single-diagonal DW crystal.

Video D. The \vec{r} -space tweed precursor: This shows dynamical tweed in the region $T_0 > T > T_d$, as an array of vibrating martensitic islands in an austenite sea, possibly induced by a \vec{k} space profile, vibrating on top of a topologically blocked bottleneck.

- ²⁸ P.G. Wolynes, Proc. of the Am. Phil. Society **145**, 4 (2001).
²⁹ M. Cieplak and I. Sulkowska, J. Chem. Phys. **123**, 194908 (2005).
³⁰ D. J. Bicout and A. Szabo, Protein Science **9**, 452 (2000).
³¹ N. Shankaraiah, K.P.N. Murthy and S.R. Shenoy, <https://arxiv.org/pdf/2111.04290.pdf>
³² KPN Murthy, *Monte Carlo Methods in Statistical Physics*, Universities Press, Hyderabad (2004).
³³ K Huang, *Statistical Mechanics* 2nd edition Wiley, NY (1987).
³⁴ P. Sollich and F. Ritort, Adv Phys., **52**, 219 (2003).
³⁵ S.R. Shenoy and T. Lookman, Phys. Rev. B., **78**, 144103 (2008). See Fig 7.
³⁶ A. Planes, F.-J. Perez-Roche, E. Vives and L. Manosa, Scr. Mater., **50** 181 (2004).
³⁷ D.W. Scott, Biometrika **66**, 605 (1979).
³⁸ G.S. Bales and R.J. Gooding, Phys. Rev. Lett., **67**, 34412 (1991).
³⁹ The mean equilibration rate is the average over an inter-shell rate $1/t(\delta E)$ over all heat releases. With a normalized PES probability, $1/\bar{t} = \int_{-\infty}^0 d\delta E P_0(\delta E, T)/t(\delta E)$. For slow intershell variation $1/t(\delta E) \simeq 1/t_0$, the mean rate is proportional to the acceptance fraction over energy decrements. Taking the PES probability, as a shifted gaussian with peak mean energy change $M > 0$, and variance $\sigma^2 = 2MT_{eff}$, the acceptance fraction is a complementary error function, whose asymptotic behaviour

yields $t_0/\bar{t} \simeq e^{-M/4T_{eff}}$. Dropping constants, the martensitic mean conversion time near T_d is written simply as $\bar{t}_m(T) = t_0 e^{1/T_{eff}(T)}$.

- ⁴⁰ U. Chandni, S Kar-Narayan, A. Ghosh, H.S. Vijaya and S. Mohan, Acta Mater., **57**,6113 (2009);
A. Planes, Ll. Manosa and E. Vives, J. Alloys and Comp., **577**, S699 (2013);
Z. Eranson, B. Ruta, S. Hechler, M. Stolpe, E. Pineda, I. Gallimo, and R. Busch, Phys. Rev. Lett., **115**, 175701 (2015). See also Physics **8**, S5121 (2015);
X. Balandraud, N. Barrara, P. Biscarin, M. Grediac, G. Zanzotto, Phys. Rev. B, **91**,174111 (2015);
B. Blaysat, X. Balandraud, M. Grediac, E. Vives, N. Barrera and G. Zanzotto, Nature Commun. Mater., **1**,3 (2020).
⁴¹ W.I.F. David, C.C. Wilson, P. P. Edwards, R. Jones, M.R. Harrison, Nature **331**, 245 (1988);
M. Uehara and S-W. Cheong. Europhys. Lett., **52**, 674 (2000);
V. Podzorov, B.G. Kim, V. Kiryukin, M.E. Gershenson and S.W. Cheong, Phys. Rev. B **64**, R140406 (2001);
V. Podzorov, C.H. Chen, M.E. Gershenson and S.W. Cheong, Europhys. Lett., **55**, 411 (2001). V. Hardy, A. Maignan, S. Hebert, C. Yaicle, C. Martin, M. Hervieu, M.R. Lees, G. Rowlands, D. McK. Paul and B. Raveau, Phys. Rev. B **68**, R220402 (2003);
V. Hardy, S. Majumdar, S.J. Crowe, M.R. Lee, D. McK. Paul, L. Herve', A. Maignan, S. Hebert, C. Martin, C. Yaicle, M. Hervieu and B. Raveau, Phys. Rev. B **69**, R020407 (2004).
⁴² Activated times $t = e^{U(T)/T}$ over rising energy barriers $U(T) = a + bT^2$ diverge at $T = 0$. The times fall for T increasing from zero, have a minimum, and then rise exponentially at large T . The minimum in $U(T)/T$ is at $T = T^* \equiv \sqrt{a/b}$. Close to T^* , the TTT curve has an 'isothermal' U-shape or nose: $t(T)/t(T^*) = e^{2(ab)^{1/2}[(T/T^*)-1]^2}$.